工學博士學位論文

Fabrication of TiO_2/SiO_2 based Inorganic Hollow Nanostructures for Energy Conversion & Storage Applications

티타니아/실리카 기반의 무기 중공 나노구조체의 제조 및 에너지 변환·저장 소재로의 응용

2018年 2月

서울大學校 大學院

化學生物工學部

尹 周 映

Fabrication of TiO_2/SiO_2 Inorganic Hollow Nanostructures for Energy Conversion & Storage Applications

2018年

尹周映

↑ 2cm ↓

↑ 2.5cm ↓

↑ 4cm ↓

↑ 3cm ↓

↑ 2cm ↓

Fabrication of TiO_2/SiO_2 Inorganic Hollow Nanostructures for Energy Conversion & Storage Applications

티타니아/실리카 기반의 무기 중공 나노구조체의 제조 및 에너지 변환·저장 소재로의 응용

指導敎授 張 正 植

이 論文을 工學博士 學位論文으로 提出함

2017 년 11 월

서울大學校 大學院
化學生物工學部
尹 周 映

尹周映의 工學博士 學位論文을 認准함

2017 年 11 月

委 員 長 _____ (인)

副委員長 _____ (인)

委 員 _____ (인)

委 員 _____ (인)

委 員 _____ (인)

Attn: President of Seoul National University

Fabrication of TiO_2/SiO_2 Inorganic Hollow Nanostructures for Energy Conversion & Storage Applications

by

Juyoung Yun

Submitted to the Graduate School of Seoul National University in Partial Fulfillment of the Requirements for the Degree of Doctor of Philosophy

February, 2018

Thesis Adviser: Jyongsik Jang

Abstract

Nanomaterials are used to develop existing fields or to pioneer new fields through superior physical properties and performance in material engineering. Particularly, the hollow nanostructures have attracted much interest in nanoscience and technology fields due to their high surface area, low density, supporting ability and light scattering. The hollow nanostructures are fabricated using convenient template methods and various other approaches. However, there are problems that need to be adjusted in size, morphology and uniformity. In addition, it is necessary to develop composite materials or add functional groups according to the needs of the application fields.

This dissertation describes the application of inorganic hollow nanostructures as materials for energy conversion and storage. Silica/titania based hollow nanostructures were prepared by sol-gel method. In the case of nitrogen-doped carbon double shell hollow nanostructures, silica/titania double shell hollow nanoparticles were first fabricated by sol-gel mehod for template and then nitrogen-doped carbon double shell nanostructures were prepared using the template method. The silica/titania based hollow nanoparticles were applied to dye-sensitized solar cells and perovskite solar cells. The large surface

area, light scattering effect and effective loading of the hollow nanostructures were used and the electron transfer effect according to the composition of the hollow nanostructure was utilized in energy conversion applications. Nitrogen-doped carbon double shell nanostructures were applied as materials for supercapacitors. The large surface area of dual structure and the oxidation-redox reaction of nitrogen doping improved the performance. As a result, the prepared inorganic hollow nanostructures improved the performance of energy conversion and storage applications.

Keywords: Nano materials, Inorganic Nanostructures, Hollow nanomaterials, Solar cells, Supercapacitors

List of Abbreviations

1D: one-dimension

A: ampere

Ag/AgCl electrode: silver chloride electrode

Ag: silver

Al-TiO_2: Al-doped TiO_2

Au: gold

Au@Ag CSNPs: Au@Ag core/shell nanoparticles

Au@Ag/TiO_2 HNPs: Au@Ag core/shell nanoparticles decorated TiO_2 hollow nanoparticles

BMII: 1-butyl-3-methyl-imidazolium iodide

BET: Brunauer-Emmett-Teller

BJH: Barrett-Joyner-Halenda

ca.: circa

cm: centi-meter

CSNPs: core/shell nanoparticles

C_s: specific capapcitance

CV: cyclic voltammetry

DSSCs: dye-sensitized solar cells

DMF: dimethyl formamide

DI: de-ionized

DRS: diffuse reflectance spectra

EDS: energy dispersive spectroscopy

EDLCs: electric double layer capacitors

EELS: electron energy loss spectroscopy

EIS: electrochemical impedance spectroscopy

eV: electron volt

F: Faraday

FE-SEM: field emission-scanning electron microscopy

FF: fill factor

FRET: fluorescence-resonance-energy-transfer

FTO: fluorine-doped tin oxide

g: gram

H_2SO_4: sulfuric acid

HNPs: hollow nanoparticles

HF: hydrogen fluoride

HR-TEM: high resolution-transmission electron microscopy

HTM: hole transport material

Hz: hertz

hr: hour

I_2: iodine

IPCE: incident photon to electron conversion efficiency

J-V curve: current density-voltage curve

J_{sc} : short circuit current

LiI: lithium iodide

LSPR: localized surface plasmon resonance

LSMs: light scattering materials

M: mole

MCs: mesoporous carbons

MDL: minimum detectable level

MFC: mass flow controller

MPTS: 3-mercapto-propyltrimethoxysilane

min: minute

mM: milli-mole

mV: milli-volt

N_2: nitrogen

NaOH: sodium hydroxide

NC DS-HNPs: nitrogen-doped carbon double-shell hollow nanoparticles

NC SS-HNPs: nitrogen-doped carbon single-shell hollow

nanoparticles

NH_4OH : ammonium hydroxide

nm: nano-meter

nM: nano-mole

NPs: nanoparticles

OA: octylamine

PCE: power conversion efficiency

PD: polydopamine

PL: photoluminescence

PSCs: perovskite solar cells

PVP: polyvinylpyrrolidone

PVDF: poly(vinylidene fluoride)

Pt: platinum

QDs: quantum dots

s: second

SiO_2: silica

SnO_2: tin dioxide

STCSNPs: SiO_2/TiO_2 core/shell nanoparticles

STS CSNPs: $SiO_2/TiO_2/SiO_2$ core/shell nanoparticles

STST CSNPs: $SiO_2/TiO_2/SiO_2/TiO_2$ core/shell nanoparticles

ST SS-HNPs: SiO_2/TiO_2 single-shell hollow nanoparticles

ST DS-HNPs: SiO_2/TiO_2 double-shell hollow nanoparticles

STEM: scanning transmission electron microscopy

STHNPs: SiO_2/TiO_2 hollow nanoparticles

TEM: transmission electron microscopy

THNP: TiO_2 hollow nanoparticles

TIP: titanium isopropoxide

Tiacac: titanium diisopropoxide bis(acetylacetonate)

TiO_2: titania

$TiCl_4$: titanium chloride

UV/vis: ultraviolet/visible

V: voltage

V_{oc}: open circuit voltage

XPS: x-ray photoemission spectroscopy

XRD: x-ray diffraction

θ: theta

μL: micro-liter

μm: micro-meter

Ω: ohm

List of Figures

c) electrochemical impedance spectra (EIS) of the NC DS-HNPs (inset: magnified region), and d) cycling performance of the NC SS-HNPs and NC DS-HNPs at a current density of 1 A g^{-1}.

Figure 50. TEM image of NC DS-HNPs after 5000 cycles at a current density of 1 A g^{-1}

List of Tables

Table of Contents

1. Introduction

1.1 Background

1.1.1. Hollow Structured Nanomaterials

1.1.1.1. Nanomaterials

Nanomaterials and nanostructures play an important role in the recent development of many areas such as physics, chemistry, material science, engineering, and biology. The various types of nanomaterials are small in size compared to bulk materials and possess new physical and chemical properties that can be applied to the wide range of energy, environmental, electronic, and biomedical applications. For example, if the size of a semiconductor material becomes smaller than a certain size, the band gap increases due to the quantum confinement effect. [1, 2] Depending on the size of the material, the band gap varies, thereby changing the optical properties. In case of novel metal, when the size is reduced to nanometer size, the color of the metal will be different from that of the bulk metal due to localized plasmon resonance. The novel metal nanoparticles have unique optical properties and exhibit excellent catalytic activity, meeting the specific requirements of the energy-related application. [3]

The broad application of nanomaterials depends not only on the new physical properties of nanomaterials, but also on the properties of nanomaterials. The increase of surface area and consequently the increase of surface energy give special performance.[4] For example, the vapor pressure, the solubility will increase exponentially with an increase in the surface area. That is, nanomaterials have much higher vapor pressure and solubility than bulk materials. In addition, when the bulk metal is reduced to a nano-size, the melting point of the metal is lowered. [5] The magnetic and electrorheology performances are also significantly improved in nano-size due to increased surface energy. [6] Nano size gives a huge advantage to the existing technical areas, it will greatly also help to open up new areas. However, nanomaterials have a negative impact on certain applications due to its small size and large surface area. For example, electrical conductivity of the nanowire is lower than a material of the bulk form due to much shortened electron mean free path.

Nanomaterials have many advantages as energy storage and energy conversion materials.[7-9] Energy storage and conversion applications involve physical or chemical interactions at the surface or interface. So, surface area, surface energy, and surface chemistry of

nanomaterials play an important role in their application. Surface energy and surface chemistry affect nucleation, growth, phase change, and thermomechanical phase behavior, not just the reaction rate. In addition, the materials, heat, and electric charge mobility of the nanomaterials is easier than the bulk material. The nanoparticles lead to new challenges in the energy storage device or conversion device. The large surface area provides more sites for charge recombination in the photovoltaic field, so efforts need to be made to solve it. In the supercapacitor, small pores in nanomaterials also interfere with electrolyte penetration.

Nanomaterials are fabricated either by top-down methods or bottom-up methods. Top-down methods can be used to produce large quantities of nanomaterials, such as ball milling, spray pyrolysis, and gas condensation. However, the top-down method has the disadvantage that it is difficult to make the size uniform. The bottom-up method, such as sol-gel method, thermal deposition, chemical vapor deposition, and colloidal synthesis, can solve these drawbacks, so that the size can be uniformly manufactured. [10, 11] The drawback of the bottom-up method is mass production. Therefore, when

manufacturing nanomaterials, these advantages and disadvantages must be considered.

Although various types of nanostructures already exist, the fabrication of nanostructures with specific functions is still important. In this dissertation, various types of inorganic hollow nanoparticles were fabricated and applied to energy conversion and storage materials. In particular, nanostructures were designed for high performance as energy conversion and storage materials.

1.1.1.2. Inorganic Nanomaterials

Over the last decades, the development of new technologies has been made possible by the manufacture or design of inorganic materials with special functions. Some of the technologies that were expected to be impossible in the fabrication of inorganic nanomaterials were made possible by advances in nanotechnology and nanoscience. Due to the development of various types of inorganic nanoparticles, technologies for energy applications such as solar cells, supercapacitors, and batteries have greatly improved. Inorganic nanomaterials such as metal oxide and carbides are prepared by various methods such as sol-

gel method, electrospinning, electrodeposition, direct oxidation, plasma oxidation, and hydrothermal method. [12]

Among them, the sol-gel method has the advantage of producing a solid-state material from a chemically uniform precursor. **Figure 1** displays general sol-gel method of metal oxides.[13] By securing the randomness of the solution state, it is necessary to produce inorganic materials such as tertiary and quaternary oxides at low process temperatures and short synthesis times by ensuring atomic bonding of the reactants. Furthermore, the sol-gel method can control the size and morphology. In fact, producing homogeneous precursors at room temperature did not guarantee homogeneity throughout the reaction. Therefore, many attempts have been made to prevent or control phase separation through sol-gel reactions. Recently, many researches have been conducted on the reaction from a gel having a certain structure in a sol-gel reaction. [14]

In addition, one-dimensional (1-D) inorganic nanomaterials are produced using electro-spinning technology. **Figure 2** exhibits the illustration of electro-spinning method. [15] The nanofibers are obtained by applying a high pressure electric field using a capillary tip to a solution containing a polymer and an inorganic precursor. In order

to obtain an inorganic nanofiber from a polymer / inorganic nanofiber, the polymer portion must be removed through a calcination process. In this way, nanofibers, nanotubes, and porous nanofibers can be fabricated. In this dissertation, inorganic hollow nanoparticles were fabricated by sol-gel method and etching process.

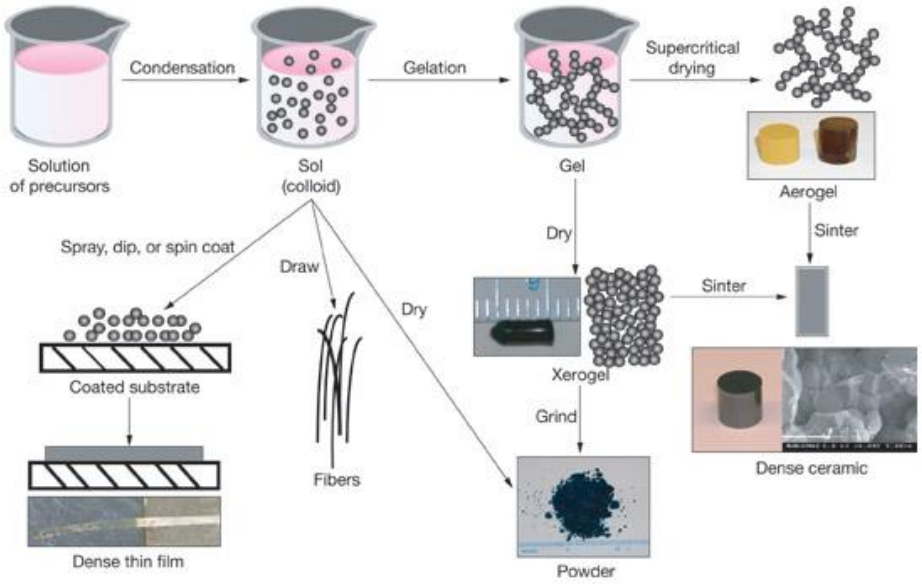

Figure 1. Schematic representation of sol-gel processing [13]

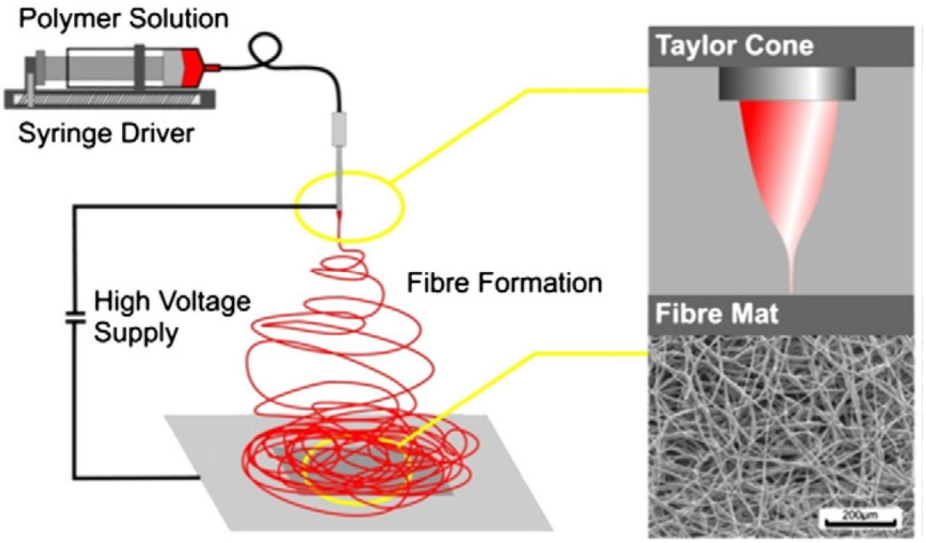

Figure 2. Illustration of electrospinning method with high voltage supply between nozzle and a grounded collector [15]

1.1.1.3. Hollow Nanomaterials

Hollow nanomaterials with well-defined morphologies have attracted attention in many areas of nanotechnology and nanoscience due to their specific properties, such as high surface area, low density, good permeability, and excellent loading capacity. These features have been applied in a variety of applications such as catalysts, sensors, energy storage, energy conversion, and drug delivery. [16-18] These hollow nanomaterials are fabricated by methods such as soft / hard template methods, Kirkendall effect, self-templating, and surface protect etching. [19, 20] However, these methods also need to solve problems such as particle / pore size, morphology control, and aggregation.

Among them, the hard template method has some disadvantages that go through several steps, but it is widely used. The general hard template method is as follow. Materials to be used as templates such as polymers or silica are first prepared. And then coating or wrapping the material to be the main component and removing the template. **Figure 3** is an example of a hollow nanoparticle fabricated by a typical hard template method. [21]

The development of hollow nanomaterials has contributed to the growth of various fields due to mechanical, chemical, optical, and

electrical properties. In this dissertation, new hard template methods were proposed to produce uniform and non-aggregated inorganic hollow nanomaterials.

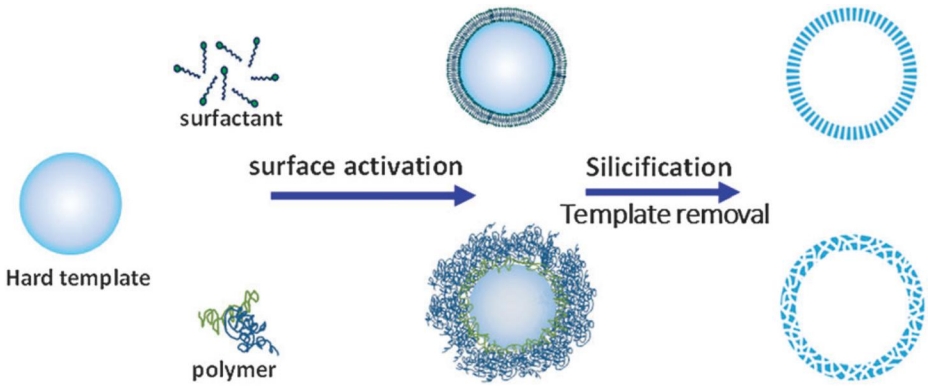

Figure 3. Scheme of hard-templating methodology for hollow mesoporous nanoparticles[21]

1.1.1.4. Carbon Hollow Nanomaterials

Carbon-based materials such as graphene[22], carbon nanofibers[23], carbon nanotubes[24], carbon spheres[25], and porous carbon[26, 27] have been studied as ecofriendly, low-cost materials for energy-related applications. Especially, nanoporous carbon materials offer large surface areas, unique structures, and high porosities[27, 28], which have enhanced the performance of various devices, including supercapacitors, lithium–sulfur batteries, nanoreactors, and cathode materials for photovoltaics, as well as catalyst supports.[29-33] The development of carbon nanostructures is a route to new solutions for these applications.

Among carbon porous materials, hollow carbon nanoparticles are of particular interest due to their low densities, unique morphologies, and pore size distributions.[34] It is essential that the hollow carbon nanoparticles have well-defined, uniform structures. They are generally fabricated using a hard template method.[35, 36] The procedure involves coating a carbon precursor on a prepared solid core template, followed by carbonization and removal of the template. This method offers the advantage of uniform fabrication; however, it can be difficult to control the morphology. Moreover, the surface of the core solid

template must be modified to ensure uniform carbon-source coating.[27] The development of new nanostructures with high surface areas using simple methods remains challenging.

In this dissertation, a new strategy to fabricate well-defined nitrogen-doped carbon double-shell nanoparticles (NC DS-HNPs) was introduced to increase the surface area for the same particle size and improve the conductivity.

1.1.2. Localized Surface Plasmon Resonance (LSPR)

Metal nanoparticles have been applied to catalysts, sensors, drugs, antimicrobials, and photonics due to their special properties such as localized surface plasmon resonance (LSPR) and surface-enhanced Raman scattering. In particular, LSPR using metal nanoparticles has been used to improve light harvesting at the photoanode. LSPR is a phenomenon that the absorption of light is amplified by resonance of the wavelength of light and the magnetic field generated around metal nanoparticles. **Figure 4** represents the phenomenon of LSPR. [37] The absorption intensity of LSPR, the plasmon bandwidth, and the stability of metal nanoparticles are important in determining the light-harvesting efficiency. Au and Ag nanoparticles have received much attention due to the excellent LSPR properties.[38, 39] Au nanoparticles have advantages of favorable stability and facile synthesis, whereas the use of Ag nanoparticles leads to a larger extinction coefficient.[40] To control the LSPR properties, control over the size, morphology, and structure of the metal nanoparticles is required.[41, 42] Particularly, proper control over the core/shell structure of Au and Ag in a single system can increase the absorption intensity, plasmon bandwidth, and stability.[43-45] In this dissertation, hollow nanoparticles with Au@Ag

core/shell nanoparticles were prepared to maximize the LSPR effect of gold and silver nanoparticles.

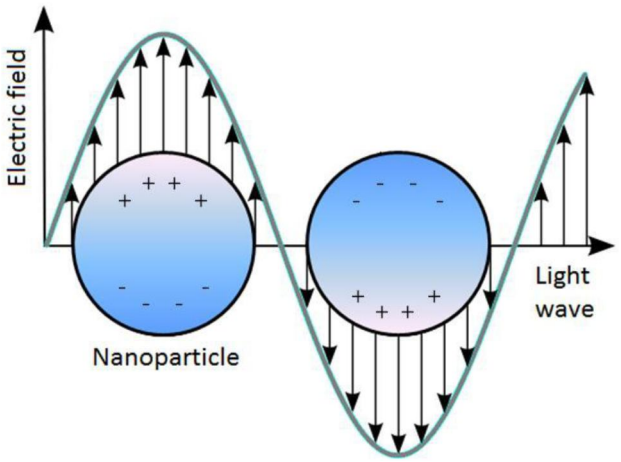

Figure 4. Schematic of localized surface plasmon resonance (LSPR) [37]

1.1.3. Application Fields

1.1.3.1. Perovskite Solar Cells

Organic-inorganic hybrid perovskites attracted the attention during the 1970-1990s, due to their unique semiconducting and conducting properties.[46] In light of the source of clean and sustainable energy, many reasearchers have long been trying to convert the solar flux to electricity through the photovoltaic properties of semiconductors. Derived from dye-sensitized solar cells (DSSCs), hybrid organic-inorganic perovskite solar cells (PSCs) have attracted attention in recent years due to their excellent properties.[47-50] Perovskite has a direct band gap that absorbs light across the entire visible solar spectrum. In addition, its exciton binding energy is small, allowing easy division into electrons and holes. Furthermore, it has higher carrier mobility and longer charge diffusion length than dyes used in DSSCs or organic photovoltaics.[51-56] PSCs can be transited into flexible, light, and low-cost energy generating device through solution process. The maximum power conversion efficiency (PCE) of perovskite solar cells has enhanced from 3.8 to 22.1 % in 7 years. Many studies have reported various approaches for improvement of the PCE, including interface engineering,[57] solvent engineering, [58,

59] design of nanostructures, [60-63] and introduction of a new charge transfer layer[64-67]. As the result, the rapid improvement of PSCs has reached the theorectical level in PCE through various innovations on film formation, interface engineering, and elemental composition, *etc*. [68-76] **Figure 5** illustrates summaries of different deposition method for high quality perovskite films.

Typical PSCs can be divided into two classes, mesoporous PSCs and planar heterojunction PSCs. **Figure 6** displays the typical structures for PSCs. [77] Mesoporous PSCs are composed of a fluorine-doped tin oxide (FTO) glass, a compact layer (electron transport layer), a scaffold layer (a nanostructured oxide layer), a perovskite layer, a hole transport layer and an Au layer. On the other hand, planar heterojunction PSCs are fabricated without scaffold layer. Effective loading of perovskite on PSCs based on insulating materials is one method for improving the efficiency of PSCs. Furthermore, the control of morphology and grain size in perovskite layer is central to improving the power conversion efficiency.

Although rapid advancement of PSCs is ongoing, many obstacles still remains and need to be overcome to prove commercial feasibility. For example, the problem of operation stability in large scale PSCs

needs to be overcome for commercialization. Perovskite is known to be vulnerable to moisture, heat, and illumination in air. Under exposure to humidity, heat, and light, PSCs had a short operational life time. For commercialization of PSCs, the resistance of these external environments should be increased. Furthermore, lead based perovskite contains Pb salt which is harmful to human.

Although these problems exist, numerous developments and discoveries have recently been achieved. The stable and eco-friendly PSCs with high efficiency are still challenging. Furthermore, the research of commercialization is needed. In this dissertation, the loading of perovskite was enhanced using hollow structures in perovskte layer, leading to improvement of the current density.

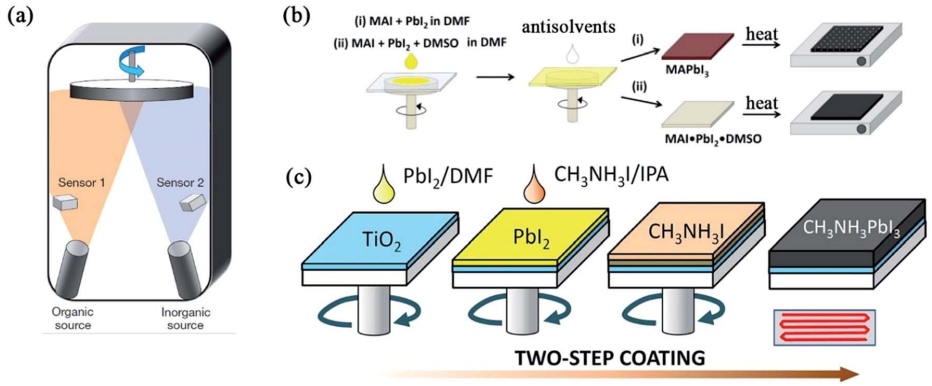

Figure 5. Summaries of different deposition methods for high quality perovskite films : (a) vapaor depositon, (b) anti-solvent engineering, and (c) two-step method. [78]

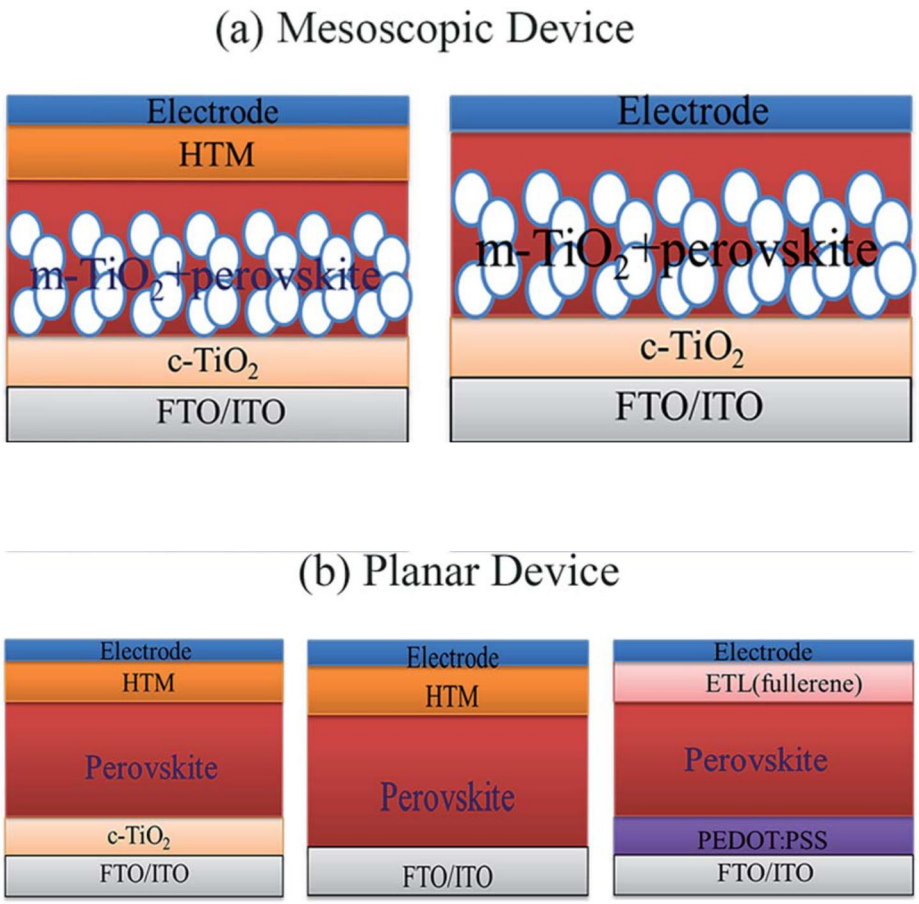

Figure 6. Structure diagram of (a) mesoscopic perovskite solar cells and (b) planar perovskite solar cells[77]

1.1.3.2. Dye-Sensitized Solar Cells

Dye-sensitized solar cells (DSSCs) have been the subject of much recent research interest due to the low costs, facile fabrication, and high power conversion efficiency (PCE).[79-81] **Figure 7** exhibits the operation principle of DSSCs. [82]In current systems, the dyes on a metal oxide absorb light in photoanode, generating electron–hole pairs and injecting electrons into the conduction band of the metal oxide. The dye is regenerated by electron transfer from an electrolyte, which is reduced at a counter electrode.[83, 84] To improve the PCE, investigations into the properties of the photoanode have been carried out because of the importance of the photoanode for light harvesting and electron transfer. Methods to improve the PCE include increased light harvesting *via* localized surface plasmon resonance LSPR,[39, 85-87] fluorescence-resonance-energy-transfer-based quantum dots (FRET-based QDs),[88, 89] TiO_2 film with high surface area to enable sufficient dye loading [90], spatial separation of cosensitization [91], the use of light-scattering materials (LSMs),[92-94] rapid electron transfer *via* 1-dimensional metal oxides,[95-97] and the use of carbon-based materials.[98, 99]

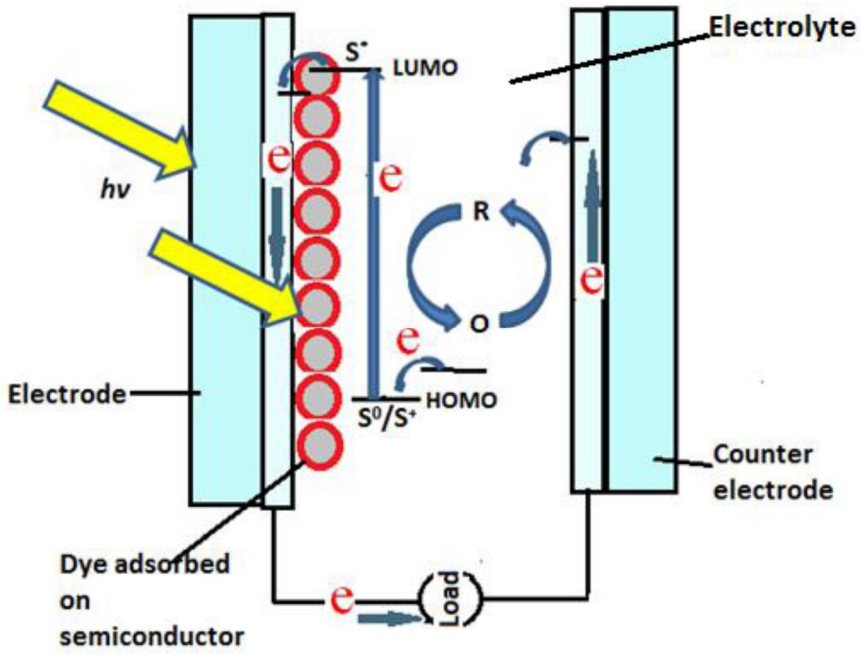

Figure 7. Schematic representation of the operating principle of a DSSCs [82]

1.1.3.3. Supercapacitors

Energy storage and conversion devices, including supercapacitors, solar cells, lithium–sulfur batteries, and fuel cells, have been developed due to increasing global pollution and energy resource shortages.[22, 100-107] Among them, supercapacitors, which can rapidly store excess electrical energy, have been implemented in many fields including portable electronics, automobile airbags, and power back-up systems.[108] Different types of supercapacitors are classified in **Figure 8**. [109] Supercapacitors have the advantages of high power density, short charging time, good stability, and ease of operation.[23, 110] Their performance depends upon the physical and chemical properties of the electrode materials. Materials with large surface areas and high conductivities improve the electrochemical performance.[22, 24]

Porous carbon materials with high surface area are promising materials for electric double layer capacitors. (EDLCs) The high surface area of porous carbon materials provides the improved property for charge accumulation, leading to high capacitance. The storage and accumulation of charge occur on a double layer at the electrode and electrolyte interface. The high surface area allows the

quick formation of double layer, resulting in high performance. The capacitance of carbon materials could be improved by heteroatom doping, providing active site which caused the pseudo capacitance. The heteroatoms and functional groups on carbon materials participate in the redox/oxidation reaction. Furthermore, these active sites improve the wettability of electrode materials. In this dissertation, nitrogen doped carbon double shell hollow nanoparticles (NC DS-HNPs) were fabricated and applied to electrode materials of supercapacitors

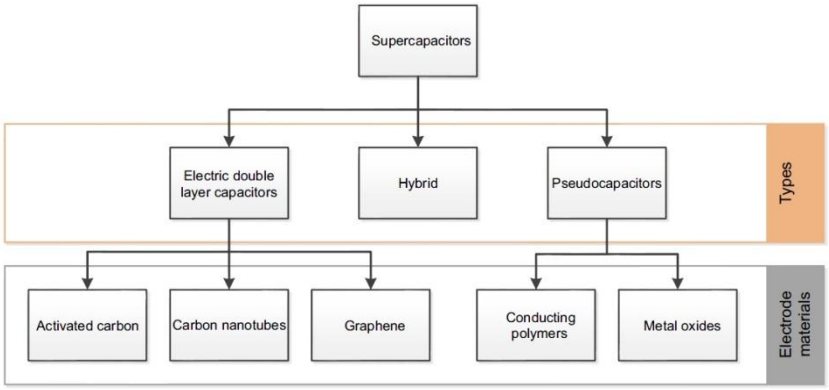

Figure 8. Classification of different supercapcitors [109]

1.2. Objectives and Outlines

1.2.1. Objectives

The aim of this dissertation is to introduce novel methods for the fabrication of various inorganic hollow nanomaterials. In detail, Au@Ag core/shell nanoparticles decorated TiO_2 hollow nanoparticles, SiO_2/TiO_2 or TiO_2 hollow nanoparticles, SiO_2/TiO_2 double shell nanoparticles, and nitrogen doped carbon double shell nanoparticles were synthesized. Furthermore, the fabricated hollow nanostructures applied in dye-sensitized solar cells, perovskite solar cells, and supercapacitors.

1.2.2. Outlines

This dissertation focused on the fabrication of inorganic hollow nanomaterials and their applications in energy field. This dissertation involves the following subtopic:

I. SiO_2/TiO_2 based hollow nanoparticles for perovskite solar cells
II. Au@Ag core/shell nanoparticles decorated TiO_2 hollow nanoparticles for dye-sensitized solar cells

III. Nitrogen doped carbon double shell nanoparticles for supercapcitors

A detailed outline of the study is as follows:

1. Perovskite solar cells (PSCs) have been developed intensively recently due to their excellent efficiency. In this study, PSCs were fabricated using a hollow structure as a scaffold layer and Al doped TiO_2 (Al-TiO_2) as a compact layer. The hollow structure exhibited effective loading of perovskite ($CH_3NH_3PbI_3Cl_{3-x}$) on the working electrode of the PSC. In particular, using SiO_2/TiO_2 hollow nanoparticles (STHNPs) instead of TiO_2 hollow nanoparticles (THNPs) as insulators improved the open circuit voltage, because STHNPs did not allow photogenerated electrons to transfer easily from the perovskite. Al-TiO_2 compact layer with low temperature procedure (≤150 °C) promoted electron extraction and reduced the recombination, leading to enhanced power conversion efficiency (PCE). An optimum PCE of 14.7% was achieved for PSCs based on STHNP scaffold layers with Al doping in the electron transfer layer. 2. Improving the light-harvesting properties of photoanodes is promising

way to enhance the power conversion efficiency (PCE) of dye-sensitized solar cells (DSSCs). The Au@Ag core/shell nanoparticles decorated TiO_2 hollow nanoparticles (Au@Ag/TiO_2 HNPs) were fabricated *via* sol-gel reaction and chemical deposition. The Au@Ag/TiO_2 HNPs exhibited multi-functions from Au@Ag core/shell NPs (Au@Ag CSNPs) and TiO_2 hollow nanoparticles (TiO_2 HNPs). These Au@Ag CSNPs exhibited strong and broadened localized surface plasmon resonance (LSPR), together with a large specific surface area of 129 m^2 g^{-1}, light scattering effect and facile oxidation-reduction reaction of electrolyte from TiO_2 HNPs, which resulted in enhancement of the light-harvesting. The optimum PCE of η = 9.7 % was achieved for the DSSCs using photoanode materials based on TiO_2 HNPs containing Au@Ag/TiO_2 HNPs (0.2 wt% Au@Ag CSNPs with respect to TiO_2 HNPs), which outperformed by 24% enhancement that of conventional photoanodes formed using P25 (η = 7.8 %).

3. Nitrogen-doped carbon double-shell hollow nanoparticles (NC DS-HNPs) were fabricated using SiO_2/TiO_2 double-shell nanoparticles (ST DS-HNPs) and polydopamine-coating. The NC DS-HNPs have a high surface area of 873.52 m^2 g^{-1} and a pore volume of 2.86 cm^3 g^{-1},

which are favorable characteristics for supercapacitor. Additionally, nitrogen doping induced pseudo-capacitance by redox activity of surface functionalities. A specific capacitance of 202 F g^{-1} was achieved for supercapacitors based on NC DS-HNPs at 0.5 A g^{-1} of current density. Consequently, the unique morphology and electrochemical properties of NC DS-HNPs display great potential for future energy-related devices.

2. Experimental Details

2.1. Fabrication of SiO_2/TiO_2 based hollow nanoparticles for perovskite solar cells

2.1.1. Synthesis of the two types of HNPs

Two types of 100 nm HNPs were synthesized using a sol-gel method and two separate etching processes. First, silica/titania core/shell nanoparticles (STCSNPs) were prepared according to a sol-gel method. A solution containing 79 mL of ethanol, 1.4 mL of de-ionized (DI) water, and 3.9 mL of ammonia solution was stirred for 1 h at 38 °C, followed by injection of 2.9 mL of tetraethyl orthosilicate (TEOS). After 10 h, the silica nanoparticles were synthesized with c.a. 75 nm diameter. Then, 3.6 mL of titanuim isopropoxide (TIP) was injected into a solution with 18 mL of acetonitrile and 54 mL of ethanol at 4 °C, which reacted with the silica nanoparticles. The STCSNPs were then separated using a centrifuge and washed with ethanol and DI water. The STHNPs were formed *via* sonication-mediated etching using an ammonia solution and STCSNPs. The THNPs were formed *via* calcination and NaOH etching. Following

etching, the two types of HNPs were isolated by centrifugation and then washed and dried in a vacuum oven.

2.1.2. Synthesis of methylammonium iodide (CH_3NH_3I)

A 30 mL HI solution (57 wt% in water, Aldrich) was reacted with 27 mL of methylamine (40 wt% in methanol, Aldrich) in a 250 mL round flask at 0 °C for 2 h, with stirring. A rotary evaporator was used to remove the solvent and obtain the precipitate. The brown methylammonium iodide (CH_3NH_3I) was washed several times using diethyl ether and dried in a vacuum oven for 24 h.

2.1.3. Synthesis of TiO_2 and Al-doped TiO_2 nanocrystals

The TiO_2 and Al-doped TiO_2 nanocrystals were synthesized *via* a non-hydrolytic sol-gel method. First, 0.5 mL of $TiCl_4$ was dropped into 2 mL of ethanol while stirring, then 10 mL of benzyl alcohol was added, resulting in yellow sol. This solution was heated at 80 °C for 8 h, leading to a white suspension. The TiO_2 crystals formed were washed with diethyl ether, then redispersed in ethanol at a concentration of 5 mg/mL. The Al-doped TiO_2 nanocrystals were synthesized using a similar method with the exception that $AlCl_3$ was added to 2 mL of ethanol at a molar ratio to $TiCl_4$. Titanium diisopropoxide bis(acetylacetonate) (Tiacac, 75% in isopropanol,

Aldrich) was then added to the solution at a concentration of 15-20 μL/mL to stabilize the crystals.

2.1.4. Assembly of perovskite solar cells

Patterned fluorine-doped tin dioxide (FTO) glass electrodes were washed using a sonication method with DI water, acetone, and isopropanol for 60 min, separately. The compact layer was spin-coated on FTO glass with a TiO_2 or Al-doped TiO_2 nanocrystal solution at 3000 rpm for 60 sec, and then annealed at 150 ℃ for 30 min in ambient air. The thickness of the compact layer was about 50 nm. A scaffold layer with a thickness of around 250 nm was deposited using spin coating. A dimethylformamide (DMF) solution (40 wt% in a mixture of 3:1 (CH_3NH_3I:$PbCl_2$)) was prepared for the perovskite layer. The perovskite solution was cast onto the substrate at 3000 rpm for 60 s, then annealed at 100 ℃ for 60 min in ambient air to form perovskite films ($CH_3NH_3PbI_{3-x}Cl_x$). The hole transfer layer was spin-coated using a 1 mL chlorobenzene solution including 72.3 mg/mL of Spiro-MeOTAD, 28.8 μL of tert-butylpyridine, and 17.5 μL of 1 mL acetonitrile solution containing 520 mg lithium bis(tri fluoromethylsyfonyl) imide salt at 3500 rpm for 50 s. Finally, an Au

counter electrode was formed by thermal evaporation. The active area was 0.09 cm^2.

2.1.5. Characterization of SiO_2/TiO_2 based HNPs in PSC

TEM and FE-SEM images were taken with a JEOL JEM-200CX and JEOL JSM6700-F. The electron energy loss spectroscopy mapping and scanning TEM/energy dispersive spectroscopy line analysis were obtained using a JEOL JEM-2100F. X-ray diffraction measurements were determined using a M18XHF-SRA (Mac Science Co., Yokohama, Japan) with a Cu Kα radiation source (λ = 1.5406 Å) at 40 kV and 300 mA (12 kW). UV-vis spectra were measured using a Lamda 35 (Perkin-Elmer). X-ray photoelectron spectroscopy measurements were taken with an AXIS-Hsi. A PerkinElmer LS 45 fluorescence spectrometer was used to provide photoluminesence measurements. EIS spectra were characterized from 0.1 Hz to 250 kHz using a Zahaner Electric IM6 analyzer. Photovoltaic parameters of PSCs were obtained using a 500 W xenon lamp with MP-160 I-V Tracer (EKO Instruments, delay time 0.005s and scan rate 1.0V/s) The incident photocurrent efficiency (IPCE; PV measurement. Inc., Boulder, CO) was characterized from 300 nm to 850 nm. (chopper frequency 4Hz, without bias light and 10 nm step wavelength)

2.2. Fabrication of Au@Ag core/shell nanoparticles decorated TiO_2 hollow structure for efficient light harvesting in DSSCs

2.2.1. Fabrication of TiO_2 hollow nanoparticles

The synthesis of the TiO_2 HNPs began with a colloidal dispersion of SiO_2 nanoparticles (0.75 g) prepared according to the Stöber method. [111] Titanium isopropoxide (TIP, 3.6 mL) was then injected in a solution with 18 mL of ethanol and 6 mL of acetonitrile. The TIP solution reacted with the SiO_2 nanoparticles *via* a sol-gel coating process for 6 hours at 4°C. The SiO_2@TiO_2 CSNPs were then isolated *via* centrifugation and washed with ethanol and DI water. The resulting SiO_2@TiO_2 CSNPs, weighing 1.7 g and with 42% yield, were calcinated at 900°C for 6 hours and then re-dispersed in 20 mL of DI water. TiO_2 HNPs were obtained *via* selective removal of the SiO_2 core by adding an aqueous solution of NaOH (2.5 M, 4 mL) to the re-dispersed solution and stirring for 6 hours. Following etching, the resulting TiO_2 HNPs, weighing 0.9 g and with 52% yield, were separated by centrifugation and then washed with ethanol and DI water.

2.2.2. Fabrication of Au@Ag/TiO_2 HNPs

Thiol-functionalized surface of TiO_2 HNPs were obtained by dispersing 100 mg of the TiO_2 HNPs in 10 mL of ethanol *via* sonication. Then, 20 μL of 3-mercapto-propyltrimethoxysilane (MPTS) and 50 μL of 28–32.4 wt% aqueous ammonia solution were added to the TiO_2 HNPs suspension. The solution was stirred using a magnetic bar for 12 hours. The MPTS-treated TiO_2 HNPs were isolated by centrifugation and washed with ethanol. To decorate the TiO_2 HNPs with Au nanoparticles, 100 mg of the MPTS-treated TiO_2 HNPs was dispersed uniformly in 100 mL of ethylene glycol, followed by the addition of 45 mg of gold chloride (in case of Ag/TiO_2 HNPs ; 50 mg silver nitrate) and 350 mg of polyvinylpyrrolidone (PVP) with a molecular weight of M_w = 55000. Octylamine (OA, 200 μL) was rapidly injected into the mixed solution at 90°C as reduction agent, and the mixture was allowed to react for 3 hours. Then, the Au/TiO_2 HNPs, weighing 129 mg and with 88% yield, were washed with ethanol. To form the Ag shell coating, the Au/TiO_2 HNPs were re-dispersed in 100 mL of ethylene glycol, and 350 mg of PVP was added, together with a systematically varied quantity of silver nitrate. Then, 100 μL of OA was rapidly injected into the mixed solution at

90°C and allowed to react for 3 hours. The Au@Ag/TiO_2 HNPs were isolated by centrifugation, washed with ethanol and DI water, and dried in a vacuum oven.

2.2.3. Fabrication of Au@Ag/TiO_2 HNPs with SiO_2 passivation layer

The Au@Ag/TiO_2 HNPs (100 mg) were re-dispersed in 10 mL of DI water together with 100 mg of PVP and stirred overnight to allow adsorption onto the surface of the Au@Ag/TiO_2 HNPs. The PVP-treated Au@Ag/TiO_2 HNPs were then centrifuged, washed, and re-dispersed in 7.9 mL of ethanol. The colloidal dispersion was then mixed with 1.4 mL of DI water, 3.9 mL of ammonia solution, and 50 μL of tetraethyl orthosilicate, stirred at 38°C for 4 hours, centrifuged, washed, and dried in a vacuum oven.

2.2.4. Assembly of dye-sensitized solar cells

To assemble the photoanode film, pastes were prepared from the P25 and TiO_2 HNPs with and without metal nanoparticles. A fluorine-doped tin oxide (FTO) glass substrate was washed using DI water, acetone, and 2-propanol and then treated with 40 mM aqueous $TiCl_4$ solution and calcinated at 450°C for 30 minutes. Photoanodes of 10-μm thickness were prepared *via* screen-printing, heated at 450°C for

30 minutes, treated with $TiCl_4$ solution, and then calcinated again under the same conditions. The photoanode films were then immersed in an ethanol-based dye solution (N719, 5×10^{-4} M) and kept at room temperature for 18 hours. The counter electrodes were prepared on the FTO glass by dropping 5 mM 2-propanol Pt (H_2PtCl_6) solution and then sintered at 400°C for 30 minutes. The photoanodes were assembled with the Pt–FTO counter electrodes into sandwich-type cells using thermal adhesive films (Surlyn, 60 μm, Dupont). The electrolyte in the sealed cell was an I^-/I^{3-} redox couple consisting of 0.6 M 1-butyl-3-methyl-imidazolium iodide (BMII), 0.1 M LiI, 0.05 M I_2, and 0.5 M *tert*-butylpyridine in acetonitrile.

2.2.5. Characterization of Au@Ag/TiO_2 HNPs

The transmission electron microscopy (TEM) images and energy dispersive spectroscopy (EDS) analysis data of nanomaterials were obtained using a JEOL JEM-200CX and JEOL JSM 6700-F. The electron energy loss spectroscopy (EELS) mapping and scanning TEM/energy dispersive spectroscopy (STEM/EDS) line analysis data were taken with JEOL JEM-2100F. X-ray diffraction measurements were carried out using an M18XHF-SRA (Mac Science Co.,

Yokohama, Japan) with a $Cu_{K\alpha}$ radiation source (λ = 1.5406 Å) at 40 kV and 300 mA (12W). Brunauer-Emmett-Teller (BET) surface areas of TiO_2 HNPs were measured using a Micrometics analyzer (ASAP 2000; Micrometics Co., Norcross, GA). The UV/Vis diffuse reflectance spectra (DRS) and UV/Vis aborption spectra were determined by A Lambda (Perkin Elmer). The photocurrent-voltage characteristics of the assembled DSSCs were investigated by 500 W Xenon lamp (XIL model 05A50KS source units). The incident photo-to-current efficiency (IPCE; PV measurement, Inc., Boulder, CO) was obtained from 300 to 800 nm under the global AM 1.5 solar emission spectrum.

2.3. Fabrication of nitrogen-doped carbon double-shell hollow nanoparticles for supercapacitors

2.3.1. Fabrication of nitrogen-doped carbon double-shell hollow nanoparticles (NC DS-HNPs)

The SiO_2/TiO_2 double-shell nanoparticles (ST DS-HNPs) template was prepared as reported previously.[112, 113] The ST DS-HNPs (200 mg) were dispersed in 300 mL of H_2O using sonication. Dopamine (180 mg) and Tris (100 mg) were added to the prepared solution and stirred for 24 h. The polydopamine (PD)-coated template was collected by centrifugation. The PD-coated ST DS-HNPs were then heated under a flow of argon gas at 800°C for 2 h to carbonize PD. The template was removed by dilute HF acid solution over 6 h to yield nitrogen-doped carbon double-shell nanoparticles (NC DS-HNPs). Following etching, the final products were isolated by centrifugation and then washed and dried in a vacuum oven.

2.3.2. Electrochemical measurements of NC DS-HNPs based supercapacitors

A NC DS-HNP-based electrode for a supercapacitor was prepared as follows. A mixture of 0.05 g of the NC DS-HNPs and 0.5mg of

poly(vinylidene fluoride) (PVDF) as a binder were dissolved in N-methyl-pyrrolidone to form a paste. Then, the paste was applied to a stainless steel mesh (area: 0.5 cm^2) and dried for 12 h at 25°C in a vacuum oven. The electrochemical properties of the NC DS-HNPs were measured using a three-electrode system composed of 1M H_2SO_4, an Ag/AgCl reference electrode and a Pt electrode. Cyclic voltammograms were obtained over a voltage range of 0 to 1.0 V at various scan rates (5–200 mV s^{-1}). Galvanostatic charge–discharge analyses were carried out over the range of 0 to 1.0 V at various current densities (0.5–10 A g^{-1}). The galvanostatic charge–discharge test at a current density of 1 A g^{-1} over 5,000 cycles was used as an indication of the stability. Electrochemical impedance spectroscopy (EIS) spectra were recorded from 0.01 Hz to 0.1 MHz using a Zahmer Elektrik IM6 analyzer.

2.3.3. Characterization of NC DS-HNPs based supercapacitors

Transmission electron microscopy (TEM) and field-effect scanning electron microscopy (FE-SEM) images were obtained using JEOL JEM–200CX and JEOL JSM6700–F instruments. The electron energy loss spectroscopy mapping and scanning transmission electron microscopy-energy dispersive spectroscopy (STEM-EDS) line analyses

were performed using a JEOL JEM–2100F instrument. X-ray photoelectron spectroscopy (XPS) measurements were carried out with an AXIS–his instrument. The Brunauer–Emmett–Teller (BET) surface area measurements and Barrett–Joyner–Halenda (BJH) pore-size distributions were obtained using an ASAP 2010 instrument. Water contact angle measurement was performed by an SDLab-200TEZD goniometer (Femtofab, Korea).

Supplementary calculations : The specific capacitance (C_s) of a working electrode is defined as the capacitance per unit mass of one electrode. The specific capacitance is given by

$$C_s = \frac{C_{electrode}}{m}$$

where $C_{electrode}$ is the capacitance of the electrode materials in the three-electrode cell system and m is the mass of the materials in the active area. For galvanostatic charge–discharge measurements, the specific capacitance is determined as follows:

$$C_s = \frac{I \times \Delta t}{\Delta V \times m},$$

where I is the discharge current, ΔV is the voltage difference of the discharge, and Δt is the discharge time.

3. Results and Discussions

3.1. Fabrication of SiO_2/TiO_2 based hollow nanostructures for scffold layer and Al-doped TiO_2 nanocrystals for electron transfer layer in perovskite solar cells

3.1.1. Fabrication of SiO_2/TiO_2 based hollow nanostructures for scffold layer

SiO_2/TiO_2 HNPs (STHNPs) and TiO_2 HNPs (THNPs) were synthesized *via* sonication-mediated and selective etching processes, respectively, on SiO_2/TiO_2 core/shell nanoparticles (STCSNPs) to create a scaffold layer in perovskite solar cells, as previously reported.[111, 114-116] **Figure 9** displays a schematic illustration of the experimental procedure for the two types of HNP (see Experimental Section). **Figure 9b-d** exhibit high resolution transmission electron microscopy (HR-TEM) images of single particles of STCSNP, STHNP, and THNP, respectively. The scaffold layers were formed from two types of HNP using spin coating, with the thickness controlled by the concentration of the HNP in a dispersed ethanol solution. Silica nanoparticles (NPs) of the same size

as the HNPs were used as a control to evaluate the effect of a hollow structure. **Figure 10a** exhibits a representative colored cross-sectional field-emission scanning electron microscopy (FE-SEM) image of the perovskite solar cells including a scaffold layer. A flat, compact electron collection layer with a thickness of about 50 nm was deposited by spin-coating. The thicknesses of the scaffold layer, perovskite layer and hole transfer layer were about 250 nm, 300 nm, and 200 nm, respectively, deposited by spin-coating. **Figure 10b-d** displays transmission electron microscopy (TEM) images of uniform STHNPs, THNPs, and silica NPs with an average diameter of 100 nm. **Figure 11** presents STEM-EDS images and STHNP line-mapping, indicating that the STHNP has a 15 nm-thick hollow structural shell composed of silica and titania. **Figure 12a** exhibits the X-ray diffraction (XRD) spectra for the STHNPs and THNPs illustrating that STHNP contained amorphous silica and titania, while THNP contained a crystalline phase of TiO_2 anatase. **Figure 10e-g** present cross-sectional FE-SEM images of devices with scaffold layers based on STHNPs, THNPs, and silica NPs, respectively. In all devices, the perovskite infiltrates deeply into the scaffold layer. The crystallinity of perovskite films on the scaffold layer is shown in **Figure 12b**.

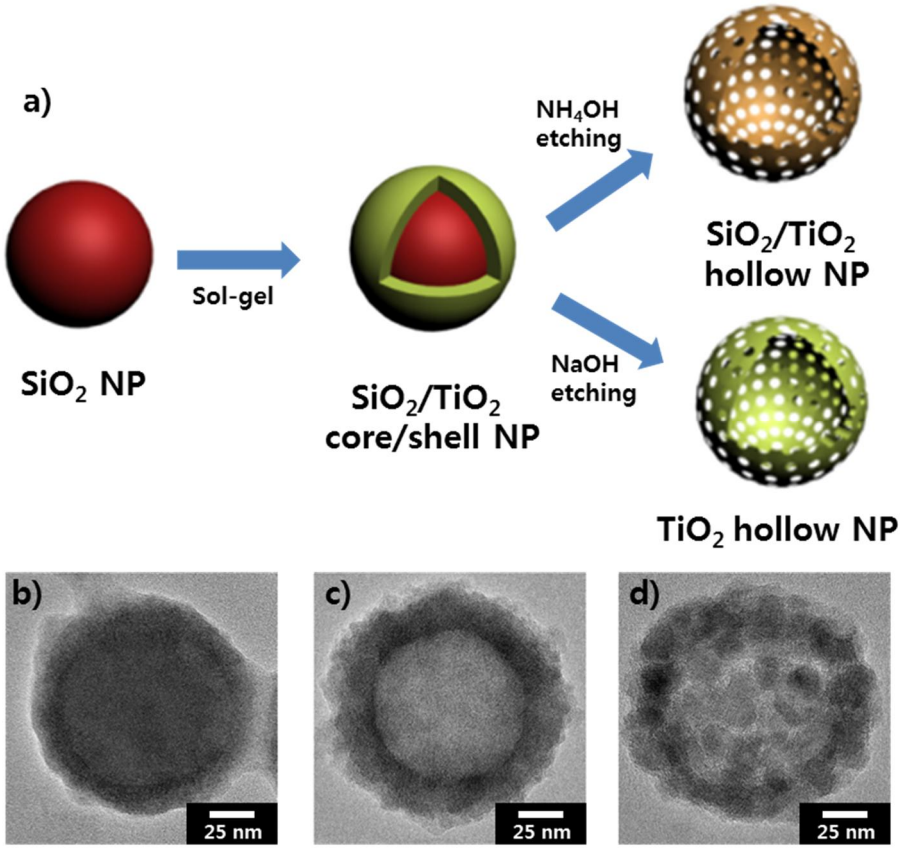

Figure 9. a) Schematic illustration of the synthesis of hollow nanoparticles. HR-TEM images of b) STCSNP, c) STHNP, d) THNP.

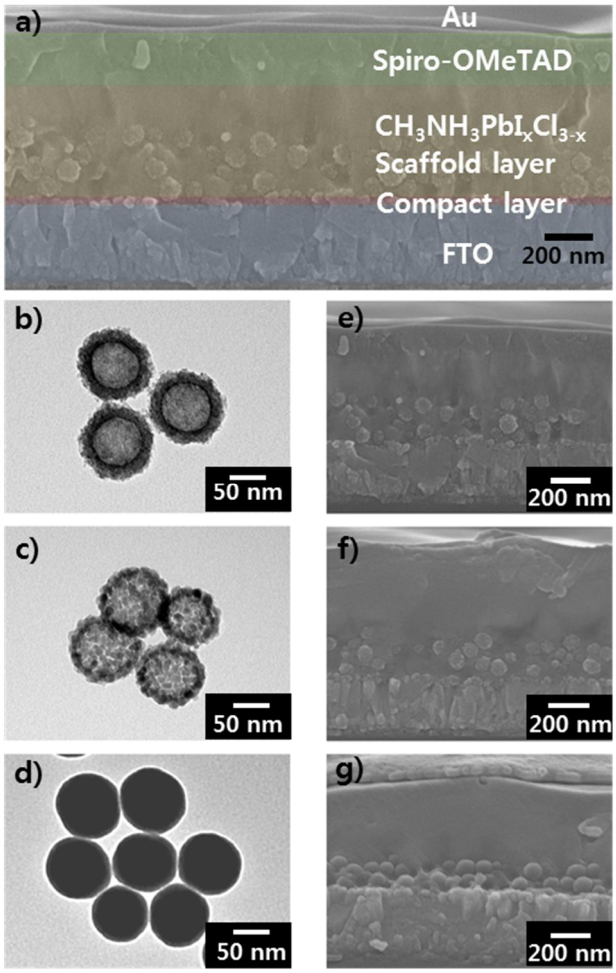

Figure 10. a) Cross-sectional FE-SEM image of perovskite solar cells. TEM images of b) STHNPs, c) THNPs, d) silica NPs. Cross-sectional FE-SEM images of perovskite solar cells based on e) STHNPs, f) THNPs, g) silica NPs.

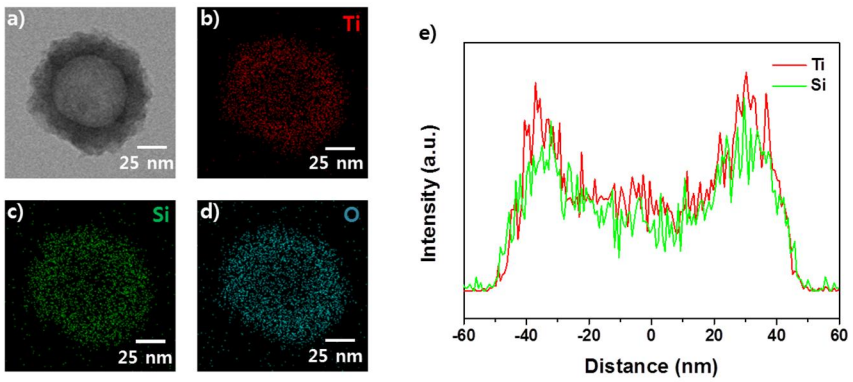

Figure 11. a) STEM images of STHNP and elemental dot mapping of b) Ti, c) Si, d) O. e) STEM-EDS line mapping of STHNP.

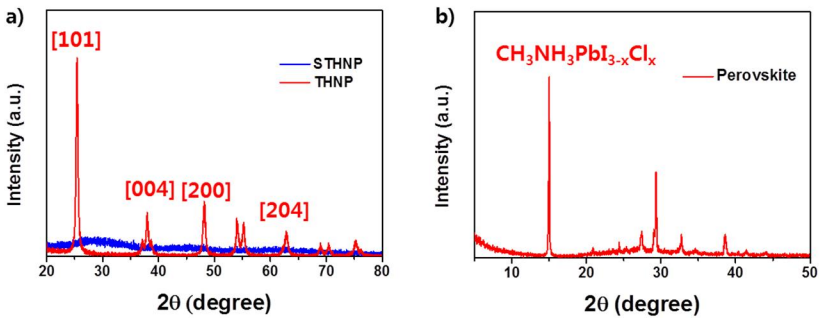

Figure 12. XRD analysis of a) STHNPs and THNPs, b) annealed perovskite films.

3.1.2. Characterization of hollow nanostructures based PSCs

Figure 13a presents UV/vis spectra for the 600 nm-thick perovskite films based on silica NPs, THNP and STHNPs to investigate the influence of the scaffold layer on the absorption of perovskite. HNP-based perovskite films absorbed better than silica NP-based film due to increased loading into the hollow inner cavity that silica NPs lack. To investigate differences between the two types of HNP, **Figure 13b** diplays photoluminescence analyses of perovskite films based on STHNP and THNP scaffolds. Because the absorptions of both HNP-based perovskite films at 500 nm were similar, PL analysis was conducted at an excitation of 500 nm. The PL emission peak of the THNPs/perovskite films was much lower than that of the STHNPs/perovskite films, implying that photogenerated electrons from the perovskite layer were quenched by electron injection into the TiO_2 anatase grain in the THNPs. The PL intensity of silica/perovskite films was lower than that of STHNPs/perovskite films due to low intensity of UV-vis spectra at 500 nm wavelength. The open circuit voltage of PSCs based on STHNPs and silica was higher than that of PSCs based on THNPs. **Figure 13c** illustrates the flow of photogenerated electrons in scaffold layers; the generated electrons

were not transported to silica NPs and STHNPs from the perovskite. The STHNPs in the scaffold layer acted similarly to Al_2O_3, ZrO_2 and SiO_2 NPs;[117-119] however, the THNP contained anatase grains which were able to transport the generated electrons from the perovskite layer. Even though the STHNPs had TiO_2, it is hard to transport electrons through STHNPs due to SiO_2. Usually, the difference of conduction band between anatase TiO_2 and perovskite was 0.1~0.2 eV. [120] From the XRD data and HR-TEM of STHNPs, there was no crystalline phase of TiO_2. The amorphous TiO_2 (3.6 eV) had larger band gap than crystalline phase (3.0~3.2 eV).[121] Furthermore, the composite of SiO_2 and TiO_2 could increase the band gap of TiO_2.[122] And, from STEM image (**Figure 11**), the distribution of Si and Ti spread evenly. As the results, the generated electrons could not be transported to the conduction band of STHNPs.

Figure 14 exhibits the photovoltaic parameters used to investigate the influence of HNPs in the scaffold layer: the short circuit current J_{sc}, open circuit voltage V_{oc}, fill factor *FF*, and power conversion efficiency (PCE). J_{sc} for devices containing both types of HNP was higher than that of devices containing silica NPs due to efficient perovskite loading enabled by the HNPs' superior structural

characteristics, as shown in the UV-vis absorption spectra. The V_{oc} measurements exhibited a different tendency from that found for J_{sc}. Silica NPs and STHNPs acted as insulators with a large band-gap, and when they were used as a scaffold material, all electronic charges resided in perovskite. The electrons were transferred in the perovskite itself. There were fewer sub-band gap states in perovskite layer than in the mesoporous TiO_2 layer.[22] As the results, V_{oc} for PSCs based on an insulating scaffold material was larger than that of PSCs based on THNPs. In addition, *FF* was influenced by the coverage of perovskite and the interface resistance. No large differences in *FF* were observed. The THNPs have an interface resistance with TiO_2 and perovskite, unlike an insulating scaffold, resulting in the lowest value of *FF*. The results demonstrate that PSC-based STHNPs had the highest PCE. **Figure 15** exhibits the *J-V* curve of the devices based on different scaffolds.

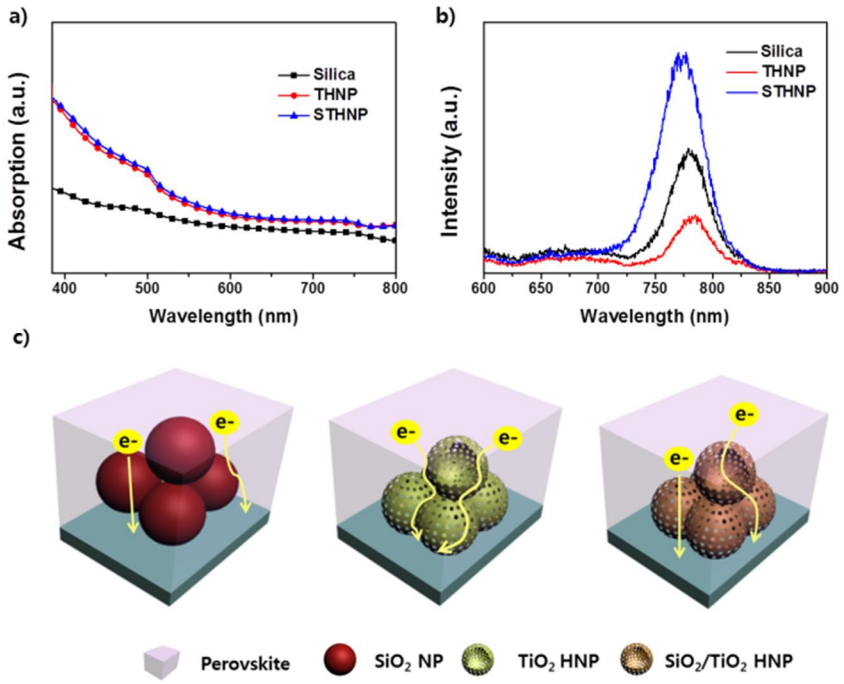

Figure 13. a) Absorption spectra of perovskite films based on silica NPs (black line), THNPs (red line), STHNPs (blue line). b) Photoluminescence spectra of the perovskite-sensitized silica NPs (black line), THNP layer (red line) and STHNP layer (blue line) (excitation at 500 nm). c) Illustration of electron transfer in perovskite films, depending on scaffold layers based on silica NPs, THNPs and STHNPs.

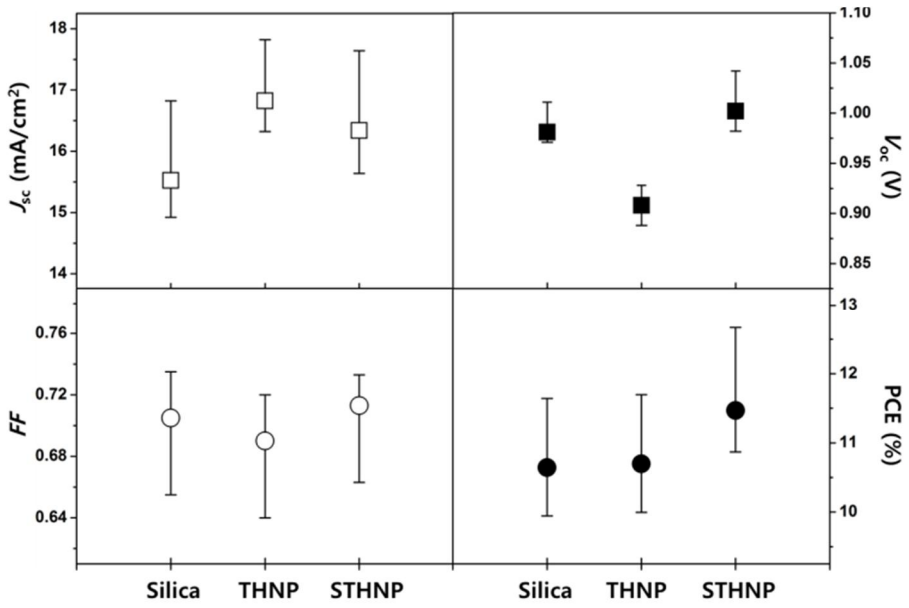

Figure 14. The photovoltaic parameters of perovskite devices based on different scaffold layers.

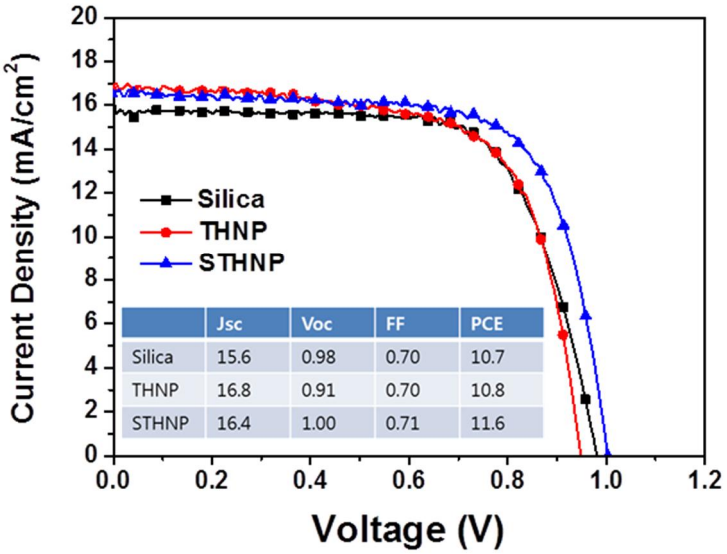

Figure 15. Current density-voltage curve of perovskite solar cells based on silica, THNPs, and STHNPs. Photovoltaic parameters are summarized in the inset table.

3.1.3. Characterization of Al-TiO_2 nanocrytals for compact layer

Al doping (2-4 mol%) in the compact layer was employed at a low sintering temperature (≤150 °C) to enhance the devices' performance **Figure 16a** exhibits the XRD analyses for unmodified and Al-doped TiO_2 nanocrystals used as a compact layer. Both peaks indicated the presence of the anatase phase of TiO_2 and no Al_2O_3. The difference of ionic radii (Al(III) = 0.53 nm, Ti(IV) = 0.61 nm) caused the small shift of peak due to small distortion by Al-doping.[123] Hence, weak doping with Al induced only a small impurity concentration, resulting in similar XRD spectra in both cases. **Figure 16b-d** display X-ray photoelectron spectroscopy (XPS) spectra for Al2p, Ti2p, and O1s for TiO_2 and Al-TiO_2 nanocrystals. The Al2p peak existed in Al-TiO_2 nanocrystals but not in TiO_2 nanocrystals, as shown in **Figure 16b**. **Figure 16c** exhibits the Ti binding energy in the anatase lattice close to 458 eV. In the case of Al-TiO_2 nanocrystals, the Ti2p peak was slightly left-shifted to a lower binding energy compared to TiO_2 nanocrystals resulting from charge transfer through Al-doping. This result may suggest that the TiO_2 lattice contained Al ions without the formation of different phases.[124] **Figure 16d** displays the O1s peaks of both nanocrystals, which were found to be similar. The major

component of the binding energy of O1s was close to 530.0 eV, corresponding to bonding with Ti and Al. The other component, with a binding energy of 531.4 eV, may correspond to hydrated bonds or carbonate bonds from surface contamination.[125] XRD and XPS data thus indicate that the compact layer was successfully doped with Al. The transmittance change of compact layer by Al-doping could effect on the current density of PSCs. **Figure 17** presents the transmittance spectra of TiO_2 and Al-TiO_2 compact layer. There was no change in the transmittance of compact layer after Al-doing (0.2-0.4 mol%) in TiO_2.

Electrochemical impedance spectroscopy (EIS) measurements were performed to characterize the kinetics of charge transfer due to Al-doping in the compact layer. **Figure 18** exhibits Nyquist plots for devices including an Al-TiO_2 compact layer and a TiO_2 compact layer under dark conditions. Usually, under dark condition, Nyquist plot implys two distinct arcs at low and higher frequency in dye-sensitized solar cells (DSSCs). In case of PSCs, the first arc is attributed to HTM transport and extraction in Au electrode at higher frequency. According to the simplified transmission line model, this first arc at higher frequencies is almost indistinguishable.[126-128] The second

arc at low frequencies is related to recombination resistance as main arc. A main arc, displaying the recombination of the charge carriers, R_{rec}, was observed in the EIS spectra. The recombination resistance of the Al-TiO_2 compact layer was larger than that of the TiO_2 compact layer. Two Al(III) substitutions with Ti(IV) eliminated oxygen defects from the TiO_2 lattice and created a favorable structure thermodynamically and electonically.[129] Thus, electrons generated in the perovskite could be transferred easily to the Al-TiO_2 compact layer. Improved electron extraction and reduced recombination were observed in the Al-TiO_2 compact layer, leading to an increase in V_{oc} and J_{sc} in perovskite solar cells. The conductivity of TiO_2 and Al-TiO_2 compact film was measured by 2-point measurement using two gold electrodes to confirm the enhancement of electronic properties.[130] The channel length and the width were 0.2 mm and 1 mm, respectively. **Table 1** certifies that the Al-doping in TiO_2 increased the conductivity. This increase could improve the carrier transport.

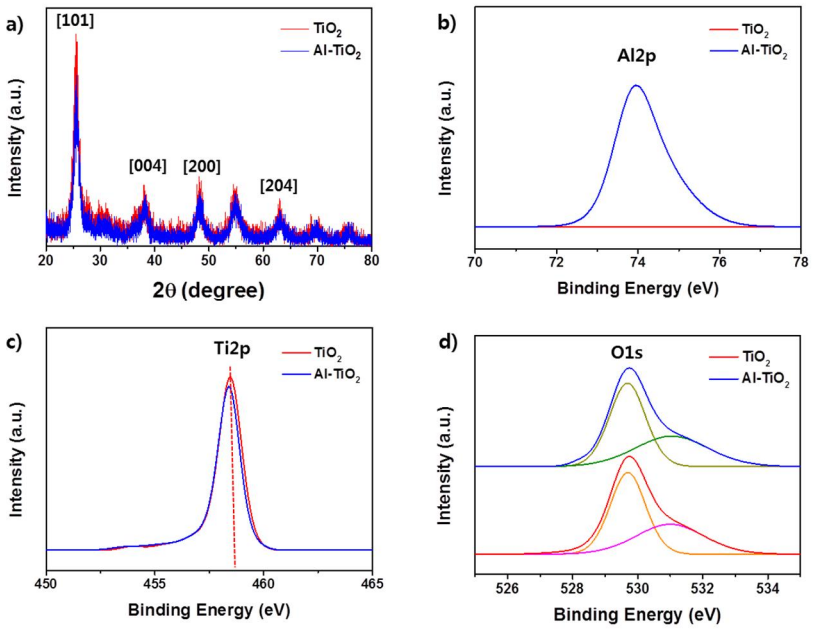

Figure 16. a) XRD analysis and b-d) XPS spectra of the TiO_2 and Al-doped TiO_2 nanocrystals used for the compact layer.

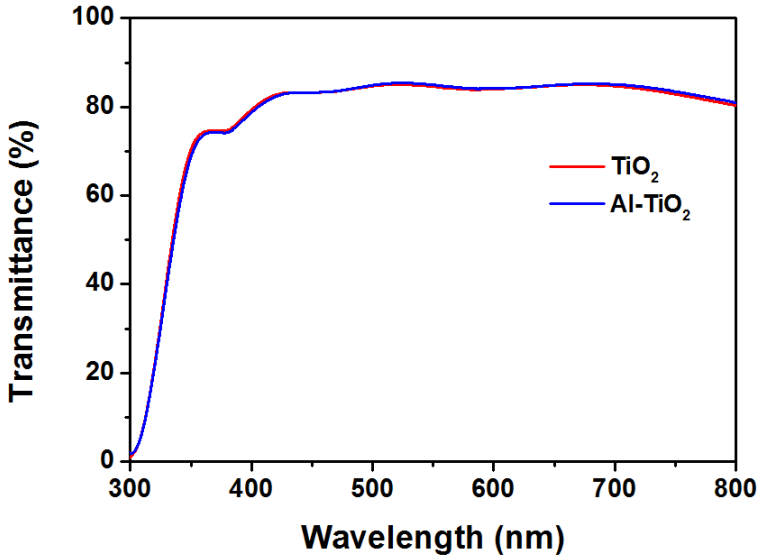

Figure 17. Transmittance spectra of the TiO_2 and Al-TiO_2 compact layer.

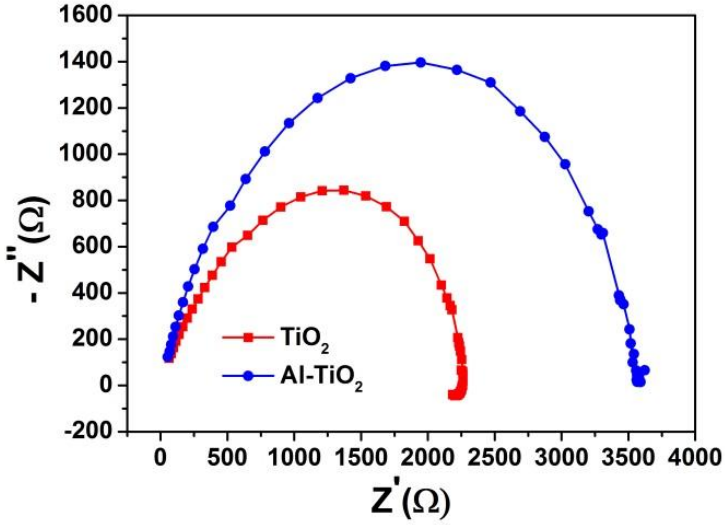

Figure 18. a) Nyquist plots of perovskite solar cells based on TiO_2 and Al-TiO_2 compact layers under dark conditions, recorded at -0.9 V.

Table 1. Conductivity of TiO_2 and Al-TiO_2 compact layer.

	TiO_2	Al-TiO_2
Conductivity (S cm^{-1})	1.58×10^{-4}	2.74×10^{-4}

3.1.4. Perfomance of Al-doped TiO_2 compact layer in PSCs

PSCs were prepared using an Al-TiO_2 compact layer with Al concentrations in the range 0-0.8 mol% to investigate the effect of doping density on performance. **Figure 19** represents the *J-V* curves and photovoltaic parameters for PSCs including an Al-TiO_2 compact layer with variable Al concentrations. The highest value of J_{sc} was exhibited for the sample containing 2-4 mol% of Al doping. An enhanced local conduction band was observed as the concentration of Al doping increased, followed by a reduction in charge injection,[131] lowering the photocurrent, J_{sc}. Thus, increasing the Al-doping concentration above 2-4 mol% decreased J_{sc} and the PCE of the PSCs. **Figure 20a** exhibits the respective J-V curves and photovoltaic parameters for PSCs based on TiO_2 and Al-TiO_2 compact layer. PSCs based on an Al-TiO_2 compact layer exhibited an enhanced photocurrent density of J_{sc} = 17.8 mA cm^{-2} and an open circuit voltage of V_{oc} = 1.05 V. These values were higher than those of PSCs based on a TiO_2 compact layer, with a photocurrent density of J_{sc} = 16.4 mA cm^{-2} and an open circuit voltage of V_{oc} = 1.00 V. Therefore, the Al-TiO_2 compact layer improved the PCE due to enhanced electron extraction and a reduced recombination rate. **Figure 20b** displays

incident photon-to-electron conversion efficiency (IPCE) spectra for PSCs based on TiO_2 and Al-TiO_2 compact layer. The enhanced electron extraction and reduced recombination rate increased the quantum efficiency at overall wavelengths. The calculated J_{sc}s from IPCE spectra were 16.3 mA cm^{-2} and 18.1 mA cm^{-2} for TiO_2 and Al-TiO_2 compact layer. These values are similar with the results in **Figure 20a**. PSCs' overall efficiency was improved through the synergistic effect of an STHNP scaffold layer and an Al-doped compact layer. **Figure 20c** displays the optimal *J-V* curve for PSC based on STHNPs and an Al-TiO_2 compact layer. Photovoltaic parameters for this device were found to be J_{sc} = 18.7 mA cm^{-2}, V_{oc} = 1.05 V, *FF* = 0.747, and PCE η = 14.7 %, under 1.5 G irradiance. This PCE value was significantly higher than that of PSCs based on silica and a TiO_2 compact layer, with a PCE of 10.7%.

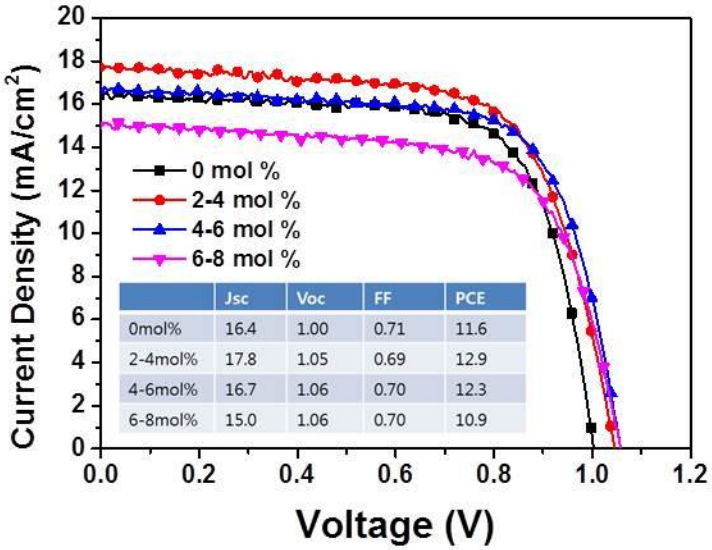

Figure 19. Current density-voltage curve of perovskite solar cells based on Al-doping concentration. Photovoltaic parameters are summarized in the inset table.

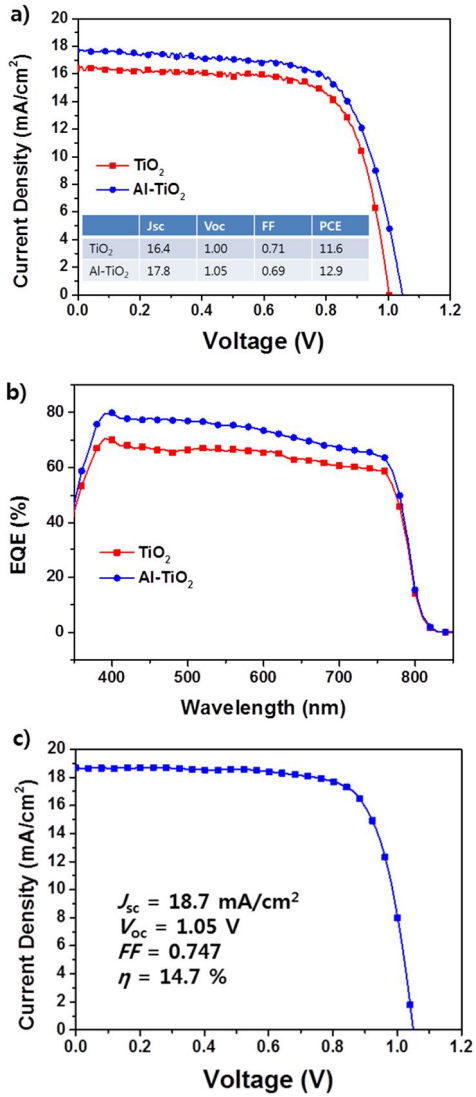

Figure 20. a) Current density-voltage curve and b) IPCE spectra of TiO_2 and Al-TiO_2 compact layer-based perovskite solar cells. The photovoltaic parameters are summarized in the inset table. c) Current density-voltage curve of the best-performing perovskite solar cells based on STHNPs as a scaffold layer and an Al-TiO_2 compact layer.

3.2. Fabrication of Au@Ag core/shell nanoparticles decorated TiO_2 hollow nanoparticles for dye-sensitized solar cells

3.2.1. Fabrication of Au@Ag core/shell Nanoparticles decorated TiO_2 hollow nanoparticles

Figure 21 exhibits an illustration of the synthesis of the Au@Ag/TiO_2 HNPs. Previously reported synthesis of SiO_2@TiO_2 core/shell nanoparticles (CSNPs) was used.[115] The SiO_2@TiO_2 CSNPs, which had an amorphous TiO_2 shell, were transformed into anatase TiO_2 HNPs *via* calcination at 900°C for 6 hours, followed by selective etching of the SiO_2 core using aqueous NaOH solution. The surface of TiO_2 HNPs was then functionalized with thiol group by using 3-mercaptopropyl trimethoxy silane (MPTS). The Au ions then were reduced and grown by a reducing agent at the surface of MPTS-treated TiO_2 HNPs *via* 1st redox deposition, due to strong affinity between the sulfur in thiol group and metal atoms.[132] The reducing agent used was octyl amine (OA), in which the alkyl chain stabilizes the nucleation and growth of metal nanoparticles. The Ag shell can then be fabricated by coating with the Au nanoparticles *via* a second redox deposition. The surface of the Au seeds act as nucleation sites

for the overgrowth of an Ag region, and the closely matched lattice constants enable a coating of Ag onto the surface of the Au nanoparticles.[133] Thus, an Ag shell can be overgrown on the Au nanoparticles epitaxially. Under the conditions described here, the thickness of the Ag shell can be tuned by controlling the amount of the Ag precursor.

Figure 22 displays transmission electron microscopy (TEM) images of the SiO_2@TiO_2 CSNPs, TiO_2 HNPs, and Au@Ag/TiO_2 HNPs. **Figure 22a** displays that the SiO_2@TiO_2 CSNPs had an average diameter of 110 ± 10 nm. The diameter of the TiO_2 HNPs was 100 ± 10 nm, as shown in **Figure 22b**; these nanoparticles had undergone calcination and a selective etching process, and during the calcination, the SiO_2@TiO_2 CSNPs shrank because the amorphous TiO_2 shells were transformed into anatase TiO_2. The TiO_2 HNPs were therefore smaller than the SiO_2@TiO_2 CSNPs. The insets of **Figure 22a** and **22b** present energy dispersive X-ray spectroscopy (EDS) data for the SiO_2@TiO_2 CSNPs and TiO_2 HNPs, respectively. The EDS analyses of the SiO_2@TiO_2 CSNPs and TiO_2 HNPs exhibit that elemental composition of Si and Ti changed from 58:42 to 2:98 following calcination and etching, and it appears that almost the entire SiO_2 core

had been removed during the etching process. **Figure 22c–f** display TEM images of Au@Ag/TiO_2 HNPs. The molar ratios of Ag and Au were 0.5:1, 1:1, 2:1, and 4:1, which named here S1, S2, S3, and S4, respectively. The Au@Ag CSNPs were larger when the Ag fraction was larger. The Ag shell of the S4 nanoparticles exhibited significant aggregation during the second redox deposition step. Unlike others, in case of S4, all Ag ions that were deposited during the second redox reaction cannot be reduced on the surface of the Au nanoparticles; hence, aggregation and side reaction occurred. With the S4 nanoparticles, Au@Ag CSNPs were not fabricated efficiently due to the loss of the Ag precursor which can be confirmed by yellow sol in the centrifuged solution. Au and Ag nanoparticles can also be decorated onto the surface of the TiO_2 HNPs separately. As a control for the S3/TiO_2 HNPs, the same amounts of Au and Ag precursor were reduced directly onto the surface of the TiO_2 HNPs separately. TEM images of the resulting Au/TiO_2 HNPs and Ag/TiO_2 HNPs exhibit that Au nanocrystals of 15 ± 5-nm and Ag nanocrystals of 25 ± 5-nm diameter formed at the surface of the TiO_2 HNPs in **Figure 23**.

Figure 24a–d display high-resolution TEM (HR-TEM) images of the nanoparticles S1–4. These images indicate a core/shell structure of

the Au@Ag CSNPs, which had Au seeds with an average diameter of 15 ± 5 nm. The Ag shell can be distinguished from the Au core in the images, appearing brighter than the Au core in HR-TEM. The thickness of the Ag shell increased as the ratio of Ag precursor to Au precursor increased. However, in the case of S4, the thickness of the Ag shell was not proportional to the amount of Ag precursor in S4, which is attributed to loss of the Ag precursor.

To investigate the elemental distribution of Au@Ag CSNPs, electron energy-loss spectroscopy (EELS) dot mapping and scanning TEM/EDS (STEM-EDS) line analysis is shown in **Figure 25**. The EELS dot mapping (**Figure 25a-d**) confirms the existence of Ag shells in the Au@Ag CSNPs. The STEM-EDS line analysis shown in **Figure 25e–h** indicates that the Au@Ag CSNPs have Au cores and Ag shells. The thickness of the Ag shell in these data is consistent with the HR-TEM analyses. The EDS analysis of Au@Ag/TiO_2 HNPs verifies the coexistence of the TiO_2 HNPs and Au@Ag CSNPs. (**Figure 26**)

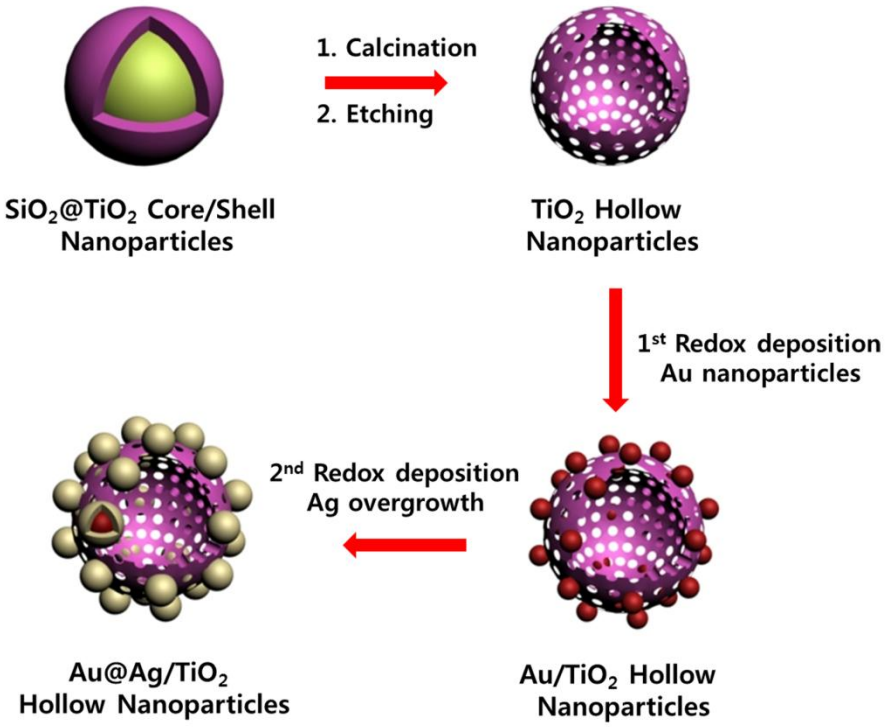

Figure 21. Schematic illustration of synthetic procedures of the Au@Ag/TiO_2 hollow nanoparticles

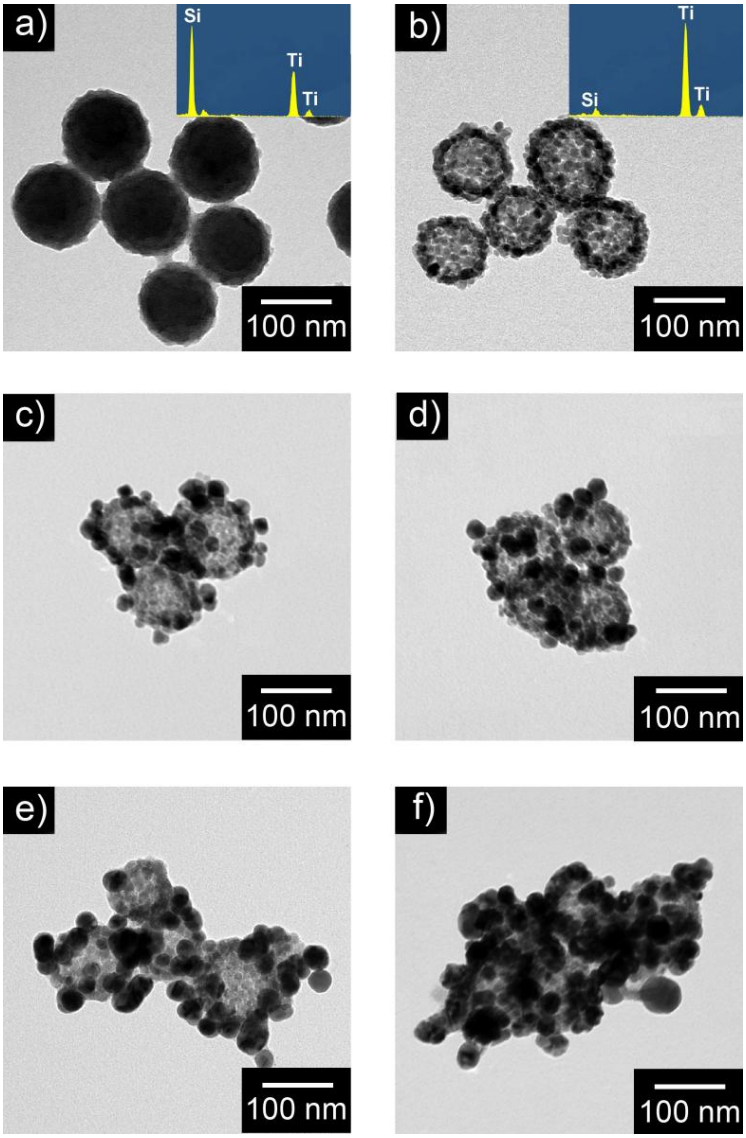

Figure 22. TEM images and EDS spectra of a) SiO_2@TiO_2 CSNPs, b) TiO_2 HNPs. c-f) TEM images of Au@Ag/TiO_2 HNPs according to precursor ratio of Ag and Au. (P_{Ag}/P_{Au} = 0.5, 1, 2, 4)

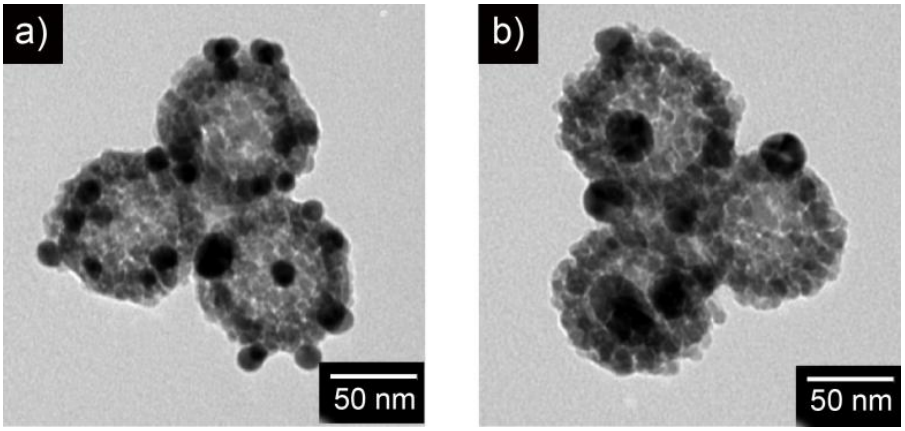

Figure 23. TEM images of a) Au/TiO_2 HNPs and b) Ag/TiO_2 HNPs. This figure exhibited Au nanoparticles with average diameter of 15 ± 5 nm and Ag nanoparticles with average diameter of 25 ± 5 nm.

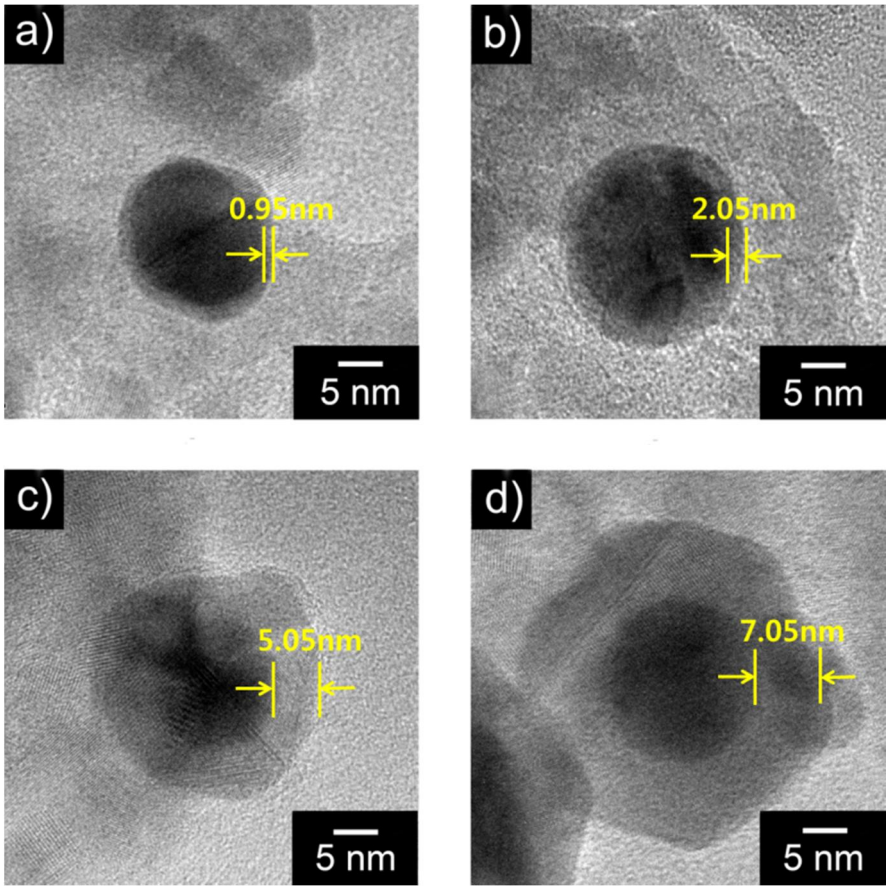

Figure 24. HR-TEM images of Au@Ag CSNPs decorated on the surface of TiO_2 HNPs with Ag shell thickness of a) 0.95 nm, b) 2.05 nm, c) 5.05 nm and d) 7.05 nm

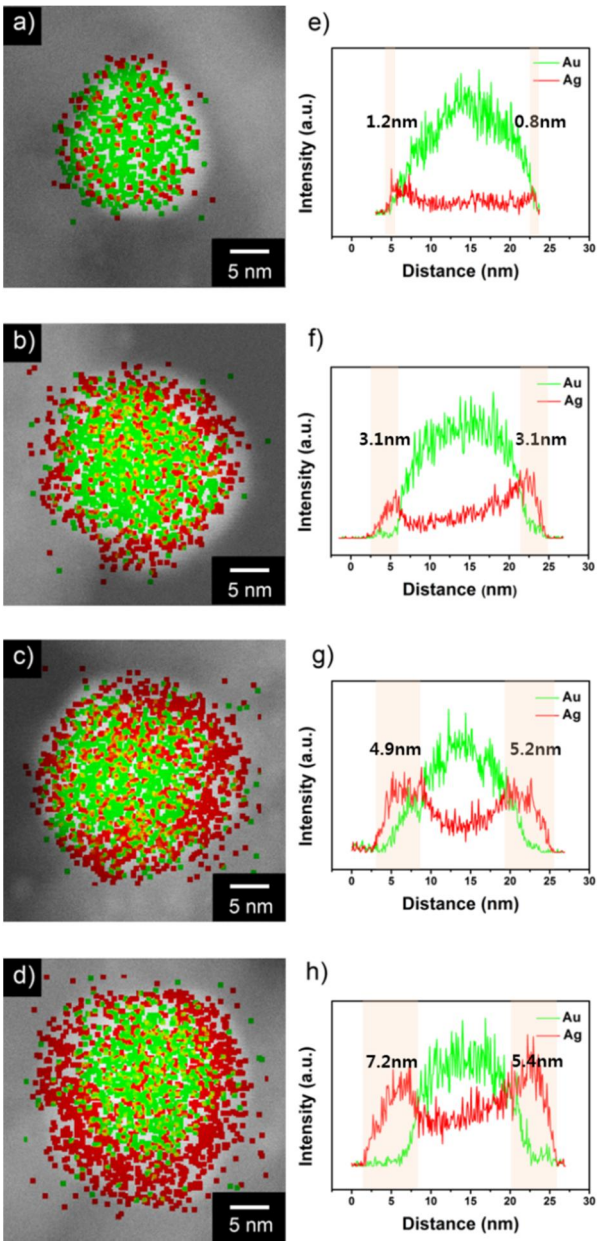

Figure 25. a-d) EELS dot mappings and e-f) STEM-EDS line mappings of S1-4. The green color represents Au, while the red color represents Ag.

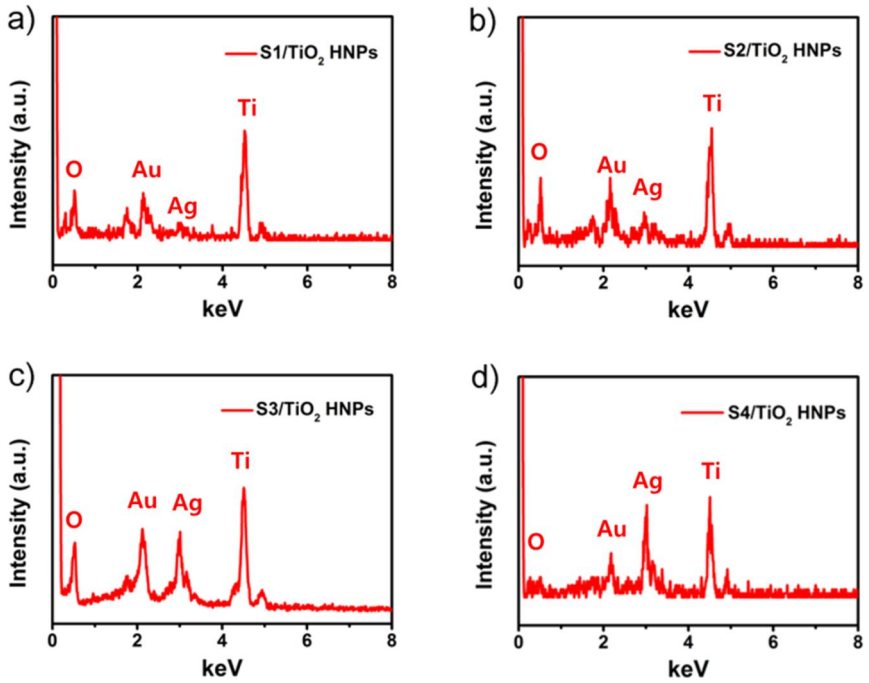

Figure 26. EDS spectra of a) $S1/TiO_2$ HNPs, b) $S2/TiO_2$ HNP, c) $S3/TiO_2$ HNP, and d) $S4/TiO_2$ HNP. As the amount of Ag precursor increase, the intensity of Ag also increases in EDS spectra.

3.2.2. Characterization of TiO_2 hollow nanoparticles

Figure 27a exhibits XRD patterns of the TiO_2 HNPs, together with those for commercially available P25 for comparison. The XRD patterns of TiO_2 HNPs exhibit peaks corresponding to the anatase phase, which has a larger electron diffusion coefficient than the rutile phase of TiO_2, which can lead to improved performance in DSSCs.[134] In the case of P25, the peaks in XRD analysis are consistent with the anatase and rutile phases, with an approximate ratio of 80:20. The inset of **Figure 27a** manifests an HR-TEM image of the TiO_2 HNPs, which indicates a lattice constant of 0.35 nm in the [101] plane. **Figure 27b** displays N_2 adsorption–desorption isotherms together with a Brunauer–Emmett–Teller (BET) analysis of the data, and **Figure 27c** presents the equivalent Barrett–Joyner–Halenda (BJH) pore size distributions for the TiO_2 HNPs and P25. In contrast to P25, the TiO_2 HNPs display type IV isotherms, which is consistent with mesoporous characteristics and a large specific surface area.[135] The specific surface area of the TiO_2 HNPs was 129 $m^2 g^{-1}$ and the specific surface area of P25 was 50 $m^2 g^{-1}$. The TiO_2 HNPs had a significantly larger specific surface area than the P25 film had, which leads to improved dye loading in DSSCs. The sharp peaks in the BJH curves

shown in **Figure 27c** for the TiO_2 HNPs indicate that these nanoparticles had pores with sizes of ~5 nm and ~35 nm. The smaller pores were distributed on the intrashell region of the TiO_2 HNPs, whereas the larger pores were located in the inner cavity of the TiO_2 HNPs. The electrolyte can diffuse into the inner cavity *via* the intrashell pores, which results in facile oxidation–reduction reactions. **Figure 27d** displays diffuse reflectance spectra (DRS) of the TiO_2 HNPs and P25. The P25 exhibited light-scattering effects because the TiO_2 nanocrystals aggregate, which may effectively reflect visible light. The 100-nm-diameter TiO_2 HNPs may also reflect the visible light *via* multiple scattering due to the hollow structure. Thus, both the TiO_2 HNPs and P25 can reflect visible light, enhancing light-harvesting properties. An increase in the optical scattering, a large dye-loading fraction, and favorable oxidation–reduction reactions of electrolyte can be expected based on these data.

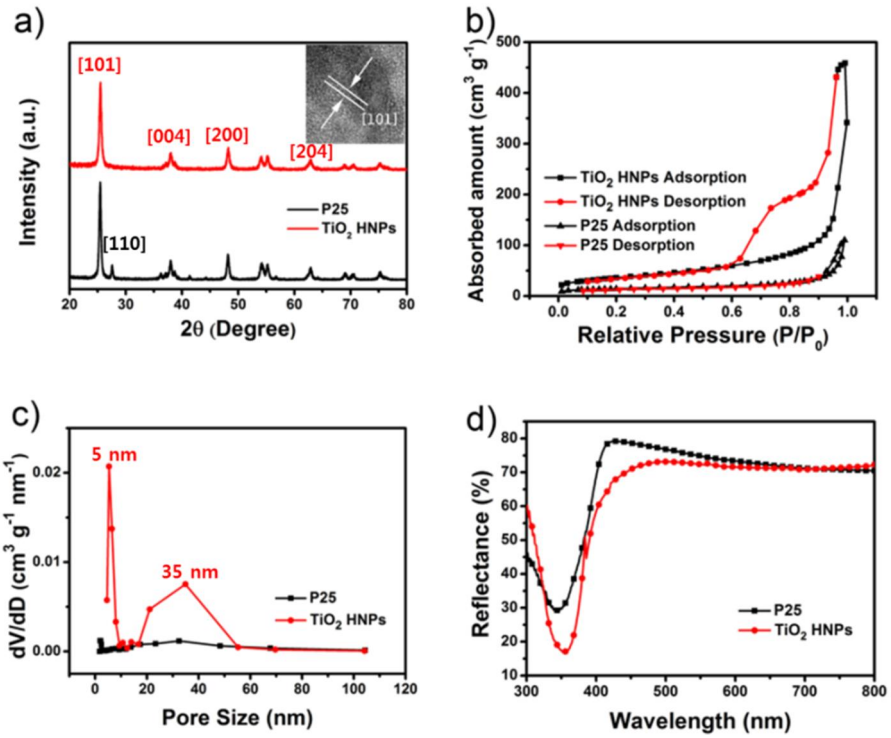

Figure 27. a) XRD patterns of TiO_2 HNPs (red line) and P25 (black line). The inset of a) is HR-TEM of TiO_2 HNPs. b) BET analysis of TiO_2 HNPs (upper curve) and P25 (lower curve). c) BJH pore size distribution and d) DRS of TiO_2 HNPs (red line) and P25 (black line).

3.2.3. The optical properties of Au@Ag/TiO_2 HNPs

Figure 28a displays UV/Vis spectra of the TiO_2 HNPs with and without the Au, Ag, and Au@Ag CSNP nanoparticles to investigate the plasmonic characteristics. The TiO_2 HNPs exhibited an absorption edge at 350 nm, and the absorption of visible light was negligible. The Au/TiO_2 HNPs and Ag/TiO_2 HNPs exhibited plasmon bands with resonance peaks at 540 nm and 440 nm, respectively. The UV/Vis spectra of the Au@Ag/TiO_2 HNPs exhibited two distinctive plasmon bands. The plasmonic characteristics of the Au core at 540 nm may be expected to be blue shifted due to the presence of high-energy resonances that coincide with the resonance of the Ag nanoparticles near 440 nm.[43] As the thickness of the Ag shell increased, a blue shift of the low-energy plasmon band occurred from 540 nm to 505 nm, as shown in **Figure 28a**. As the Ag shell became thicker, the blue-shifted low-energy plasmon band became weaker and converged to the resonance of the Ag nanoparticles due to blocking of the plasmon excitation of the Au core by the thick Ag shell. Compared with the Ag/TiO_2 HNPs, the S2/TiO_2 HNPs, although fabricated using the same total molarity of the precursor, exhibited a broader plasmon band with similar intensity. The Au@Ag CSNPs have a synergetic effect in

terms of the optical properties because of the interaction between the high-energy and low-energy plasmon bands. This synergetic effect cannot be considered as a linear combination of the individual contributions of Au core and Ag shell plasmon resonances and is instead attributed to an interaction between the core and the shell of Au@Ag CSNPs,[136] i.e., plasmon hybridization.[137] The increase in the amount of the Ag precursor did not significantly influence the form of spectra; however, according to Mie theory, it can be expected to result in stronger absorption owing to an increase in the size of the metal nanoparticles. Contrary to others, the absorption spectrum of S4 displays a slightly higher absorbance than that of S3, which is attributed to loss of Ag precursor, as described earlier. To investigate the effect of the composition of the nanoparticles on the absorption, UV/Vis spectra of a mixed solution of ruthenium dye and samples were obtained, which were measured with an accurately controlled concentration (2.5×10^{-5} M) of the dye and of the nanoparticles (5×10^{-3} M), as shown in **Figure 28b**. The UV/Vis spectra of the pure dye in ethanol (EtOH) exhibited two peaks, at 380 and 530 nm. When the dye solution was dispersed with the TiO_2 HNPs, the intensity of the peak at 380 nm increased due to absorption by the TiO_2 HNPs around

300 nm. The Au/TiO_2 HNPs and Ag/TiO_2 HNPs increased the absorption due to the LSPR of the Au and Ag nanoparticles. As the plasmon band became broader due to the presence of the Au@Ag CSNPs, the absorbance of the nanoparticle/dye dispersion was larger than that of Au/TiO_2 HNPs and Ag/TiO_2 HNPs. In particular, the S2/TiO_2 HNPs, which exhibited a similar intensity of the plasmon band and had the same molarity of Ag precursor as the Ag/TiO_2 HNPs, also exhibited an absorption coefficient that was significantly larger than that of the Ag/TiO_2 HNPs in the visible light region. The addition of metal nanoparticles to the dye solution can increase the efficiency of dye excitation or act as a sensitizer *via* coupling of the LSPR due to the metal nanoparticles and the photogeneration of electron–hole pairs in the TiO_2 HNPs.[138] Based on these data, the introduction of the Ag shell could cause the plasmon band to exhibit stronger and broader absorption, which can be expected to increase the photocurrent in DSSCs.

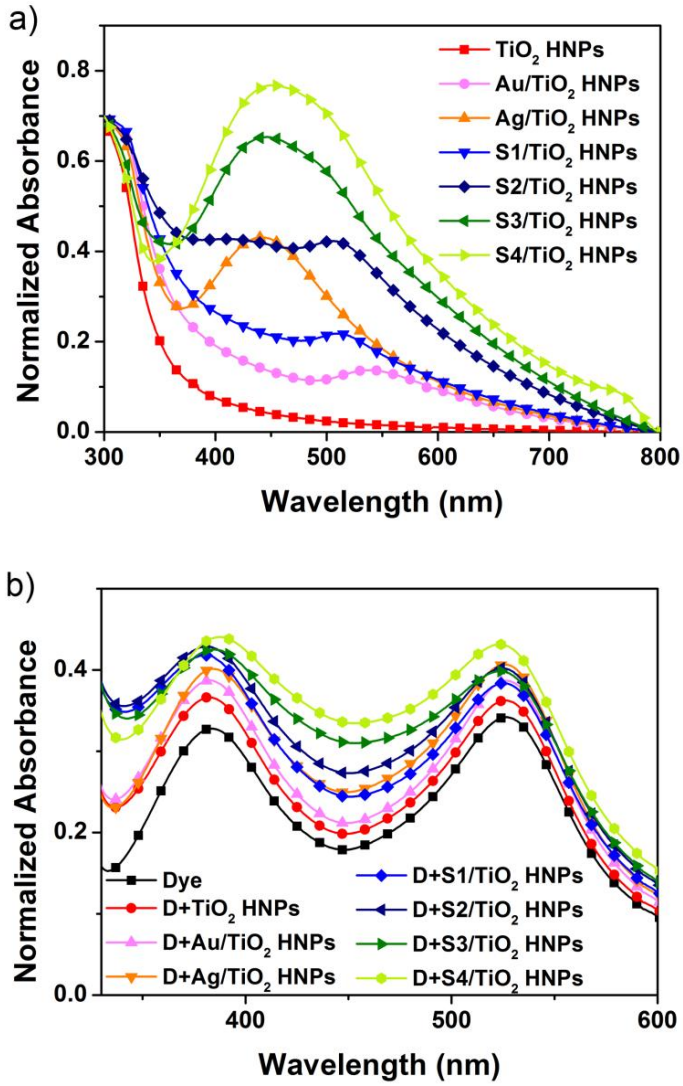

Figure 28. a) UV/Vis absorption spectra of the TiO_2 HNPs and metal nanoparticles-decorated TiO_2 HNPs. (metal nanoparticles : Au, Ag, Au@Ag CSNPs) b) Absorption spectra of the TiO_2 HNPs and metal nanoparticles-decorated TiO_2 HNPs with dye in EtOH.

3.2.4. Effect of hollow structure and LSPR of Au@Ag/TiO_2 HNPs on DSSCs

Figure 29a illustrates a schematic diagram of the structure of a DSSC incorporating Au@Ag/TiO_2 HNPs. The photoanode film consists of dye-adsorbed TiO_2 HNPs and Au@Ag/TiO_2 HNPs. **Figure 29b** exhibits a magnified image of the Au@Ag/TiO_2 HNPs, indicating the LSPR, multiple scattering, and large specific surface area. These properties can be expected to improve the light-harvesting properties.

To investigate the effects of the Au@Ag/TiO_2 HNPs coated with SiO_2 on the performance of DSSCs, the film thickness and the ratio of the metal nanoparticles to the TiO_2 HNPs were controlled. The power conversion efficiency (PCE) of all samples was averaged after 15 times of experiments under same conditions. All PCE in this paper were averaged by repeated experiments to provide the evidence for the improvement. To prevent corrosion of the Au@Ag CSNPs due to the iodide electrolyte in the DSSCs, a thin passivation layer of SiO_2 was coated onto the Au@Ag/TiO_2 HNPs using the Stöber method (**Figure 30**).[111] The introduction thin layer of SiO_2 led to a red shift of the plasmon band, as shown in **Figure 31**. This small red shift of LSPR band is caused by the reflective index of SiO_2 shell. In case of metal

core particles with smaller than 30 nm, LSPR band mostly is affected by the refractive index of SiO_2 shell, accompanied with a red shift owing to presence of multipole effects.[139] To examine the effects of the TiO_2 HNPs in DSSCs, the performance of DSSCs based on TiO_2 HNPs were compared with that of DSSCs based on P25. The DSSCs based on TiO_2 HNPs exhibited an enhanced photocurrent density of J_{sc} = 15.8 mA cm^{-2} and power conversion efficiency (PCE) of η = 8.3%; this is an improvement on the metrics for P25 (J_{sc} = 14.1 mA cm^{-2} and η = 7.8%) as shown in **Figure 32a** and **32b** and listed in **Table 2**. **Figure 33** displays the histogram displaying the distribution of PCE of each sample in Table 1. The DSSCs based on TiO_2 HNPs exhibited improved PCE due to the larger specific surface area, multiple scattering effects, and improved oxidation–reduction of the electrolyte due to the hollow structure. UV/Vis spectra of dye solution desorbed from each film are shown in **Figure 34a**. The large absorption means that the film has a large specific surface area. The film based on the TiO_2 HNPs exhibited a larger specific surface area than that of the P25. Additionally, to investigate the LSPR effect of the Au@Ag CSNPs on the performance of DSSCs, the S3/TiO_2 HNPs were examined, which exhibited a particularly strong plasmon band and negligible loss of the

Ag precursor. A TiO_2 HNPs film using the S3 HNPs was prepared with content in the range 0–0.4 wt% to determine the optimum conditions. The amount of Au@Ag CSNPs was calculated from the ratio of the quantity precursor used to form the Au seed to that used to form the Ag shell, assuming that all of the precursors reacted. The efficiency is indicated by the current-voltage (*J-V)* curves displayed in **Figure 35a** and the data listed in **Table 3**. The histogram statistics related to PCE of each condition was shown in **Figure 36**. The PCE and current density of the DSSCs increased as the amount of Au@Ag CSNPs increased up to 0.2 wt%, and decreased with larger fractions on the Au@Ag nanoparticles. An excess of the Au@Ag CSNPs may lead to increased trapping of photogenerated electrons as well as increased optical absorption, which may convert part of the incident energy to heat.[140] The open circuit voltage (V_{oc}) also slightly increased with the addition of silica coated Au@Ag/TiO_2 HNPs. Because a small quantity of insulating silica thin layer on Au@Ag/TiO_2 HNPs functions as retarding electron recombination at photoanode interfaces.[141] To further investigate the effects of the LSPR, the concentration of nanoparticles at 0.2 wt% was fixed. **Figure 32a** exhibits the photocurrent density, and **Figure 32b** displays

the PCE of each of the DSSCs based on each of the samples. The *J-V* curves are also shown for each of the samples in **Figure 35b**. The DSSCs formed using Au/TiO_2 and Ag/TiO_2 exhibited larger PCE and current densities than did those based on Au/TiO_2 HNPs. This is attributed to the stronger intensity of the plasmon bands for the Ag nanoparticles compared with the Au nanoparticles. DSSCs formed using Au@Ag/TiO_2 HNPs exhibited photocurrent density and PCE that increased from samples S1 to S3 and then decreased for sample S4. The DSSC based on S3/TiO_2 exhibited the largest photocurrent density and PCE due to the intense and broad plasmon band. Sample S4 had the highest intensity plasmon band; however, this enhanced optical absorption may result in part of the solar energy's being lost as heat. Furthermore, aggregation of metal nanoparticles could lead to a reduction in plasmonic activity. **Figure 34b** manifests absorption spectra of the dye solution desorbed from the film with and without the S3/TiO_2 HNPs. These data suggest that the presence of Au@Ag CSNPs in the film does not significantly affect the dye loading. Thus, the enhanced efficiency of the Au@Ag CSNPs is attributed to surface plasmon resonance. DSSCs based on the S3/TiO_2 HNPs exhibited photocurrent density of J_{sc} = 17.3 mA cm^{-2} and PCE of η = 9.4%,

which are larger values than those for the DSSCs based on TiO_2 HNPs, where J_{sc} = 15.8 mA cm^{-2} and η = 8.3%. **Figure 32c** displays representative *J-V* curves for DSSCs based on P25, TiO_2 HNPs, and S3/TiO_2 HNPs. These data help us to gain insight into the above-mentioned effects. The incident photon-to-electron conversion efficiency (IPCE) is shown in **Figure 32d**. The increased specific surface area of the TiO_2 HNPs increased the quantum efficiency at wavelengths in the range 400–800 nm. At wavelengths shorter than 400 nm, the DSSCs based on P25 exhibited increased quantum efficiency, which is attributed to more effective light scattering. Furthermore, the tuned LSPR effect of the Au@Ag CSNPs enhanced the quantum efficiency at wavelengths in the range 350–650 nm. These results suggest that the S3/TiO_2 HNPs are promising photoanode materials for DSSCs applications because of larger specific surface area, favorable optical scattering, facile oxidation–reduction profiles of the electrolyte, and the strong and broad LSPR.

By exploiting the large specific surface area, optical scattering, facile oxidation–reduction of the electrolyte, and strong LSPR of the Au@Ag/TiO_2 HNPs, the PCE of DSSCs could further be enhanced. **Figure 37** exhibits a *J-V* curve of a DSSC based on S3/TiO_2 HNPs.

The J_{sc} = 18.2 mA cm^{-2}, V_{oc} = 0.754 V, FF = 71%, and PCE of η = 9.7% were obtained with an irradiance under 1.5 G, i.e., solar light intensity. This value of PCE was 24% larger than the PCE of the DSSC based on P25.

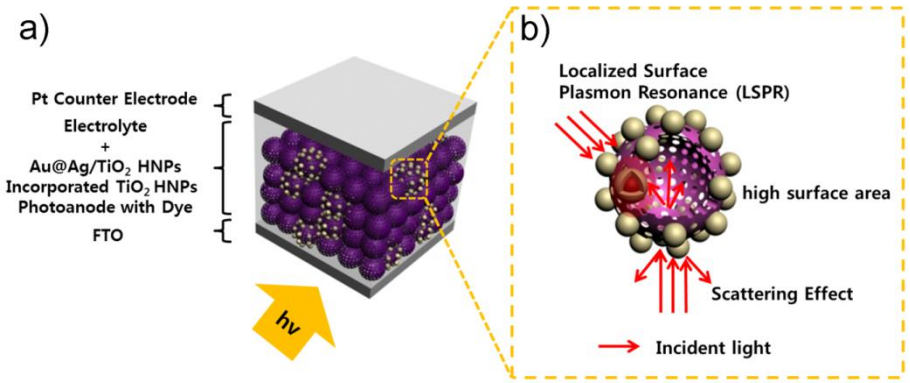

Figure 29. a) Schematic illustration of Au@Ag/TiO_2 HNPs-incorporated photoanode in TiO_2 HNPs-based DSSC b) A magnified structure of an Au@Ag/TiO_2 HNPs.

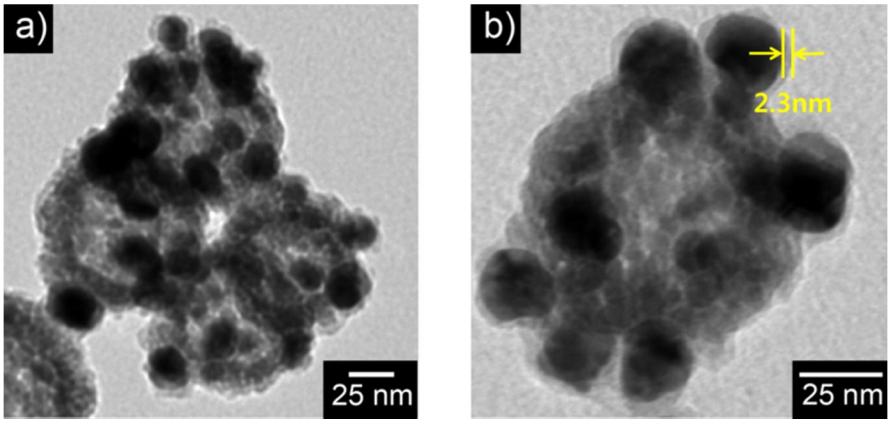

Figure 30. TEM image of a) Au@Ag/TiO_2 HNPs with SiO_2 layer and b) magnifed Au@Ag/TiO_2 HNP with SiO_2 layer.

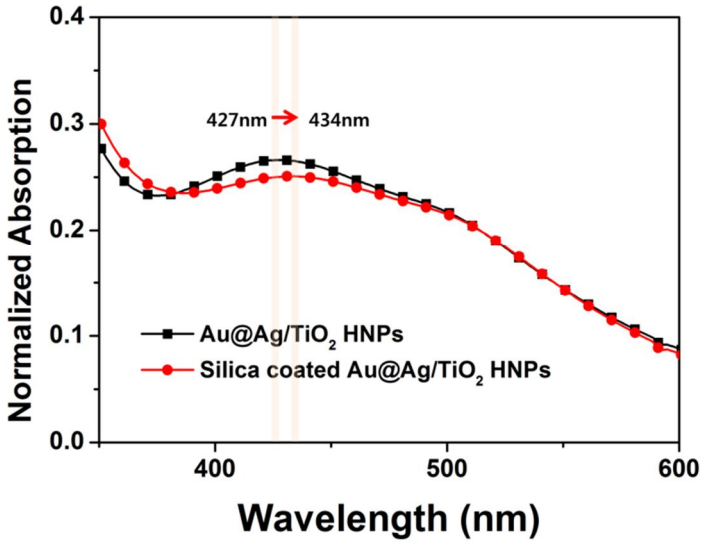

Figure 31. UV- vis spetra of Au@Ag/TiO_2 HNPs (black line) and Au@Ag/TiO_2 HNPs with SiO_2 coating (red line).

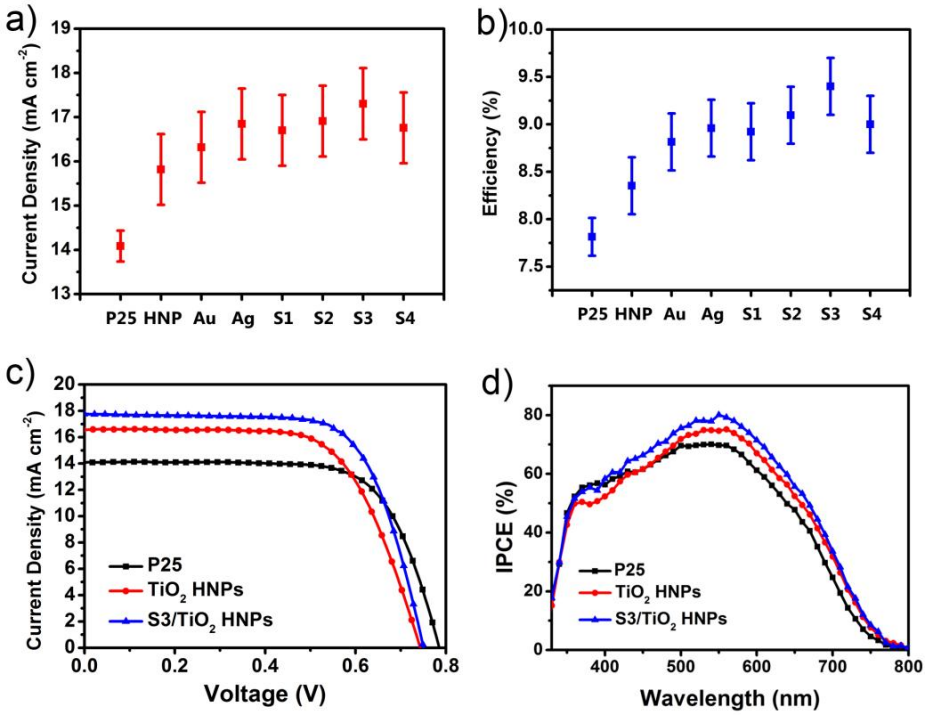

Figure 32. a) Short-circuit current and b) PCE of DSSCs using P25, TiO_2 HNPs and blend of TiO_2 HNPs and metal nanoparticles-decorated TiO_2 HNPs. (0.2wt% metal nanoparticles with respect to TiO_2 HNPs) c) Representative *J-V* curves and d) IPCE spectra for P25, TiO_2 HNPs and TiO_2 HNPs incorporating S3/TiO_2 HNPs (0.2 wt% Au@Ag CSNPs with respect to TiO_2 HNPs).

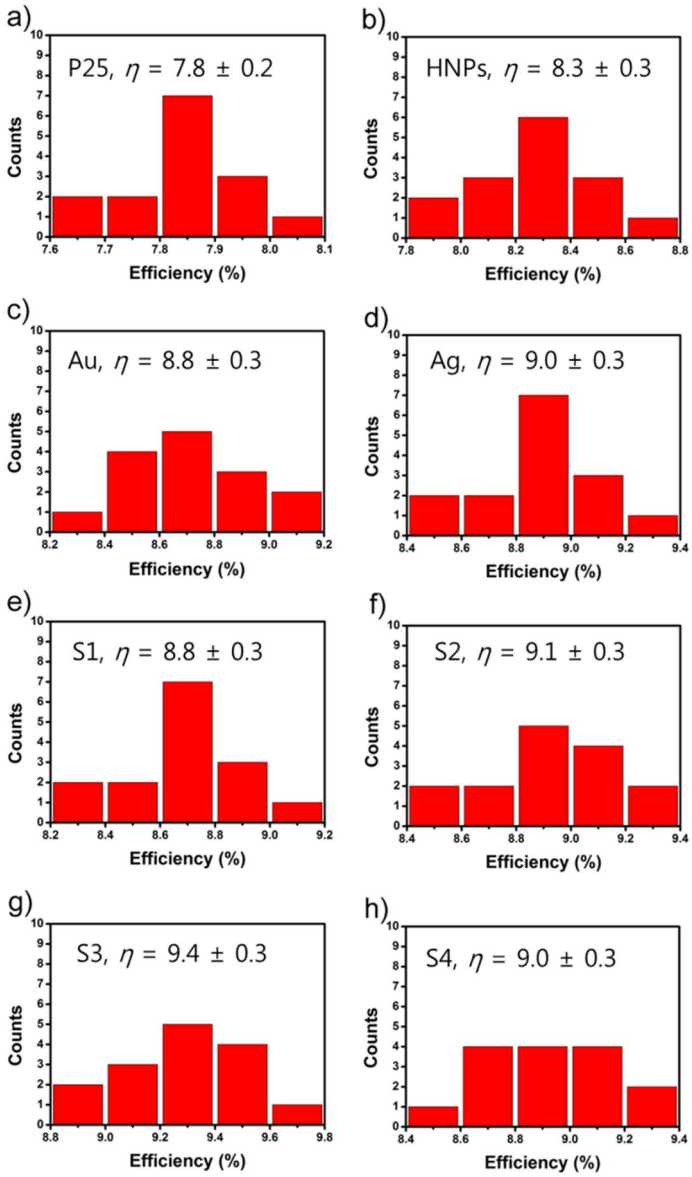

Figure 33. Histograms of power conversion efficiency for DSSCs based on a) P25, b) TiO_2 HNPs, c) Au/TiO_2 HNPs, d) Ag/TiO_2 HNPs, e) S1/TiO_2 HNPs, f) S2/TiO_2 HNPs, g) S3/TiO_2 HNPs, f) S4/TiO_2 HNPs with same amount of metal (0.2 wt%), composed of 15 separate device.

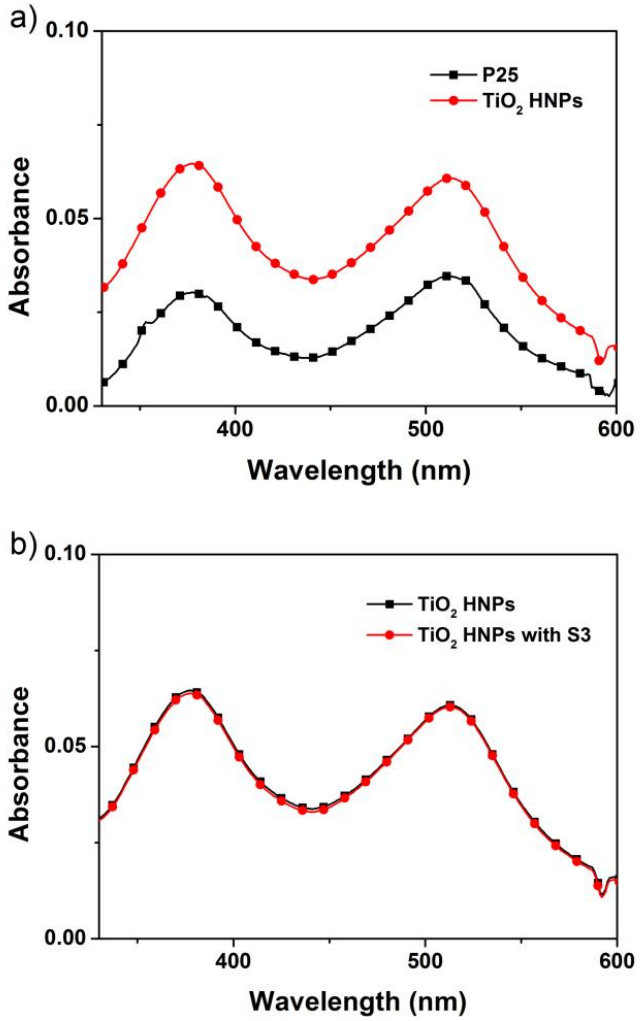

Figure 34. Absorption spetra of N719 in NaOH mixed solution (0.01 M of NaOH aqueous solution / ethanol = 1:1, v/v) desorbed from photoelectrode based on a) P25 (black line), TiO_2 HNPs (red line). b) absorption spectra with same condition based on TiO_2 HNPs(black line) and TiO_2 HNPs with silica coated Au@Ag/TiO_2 HNPs(red line).

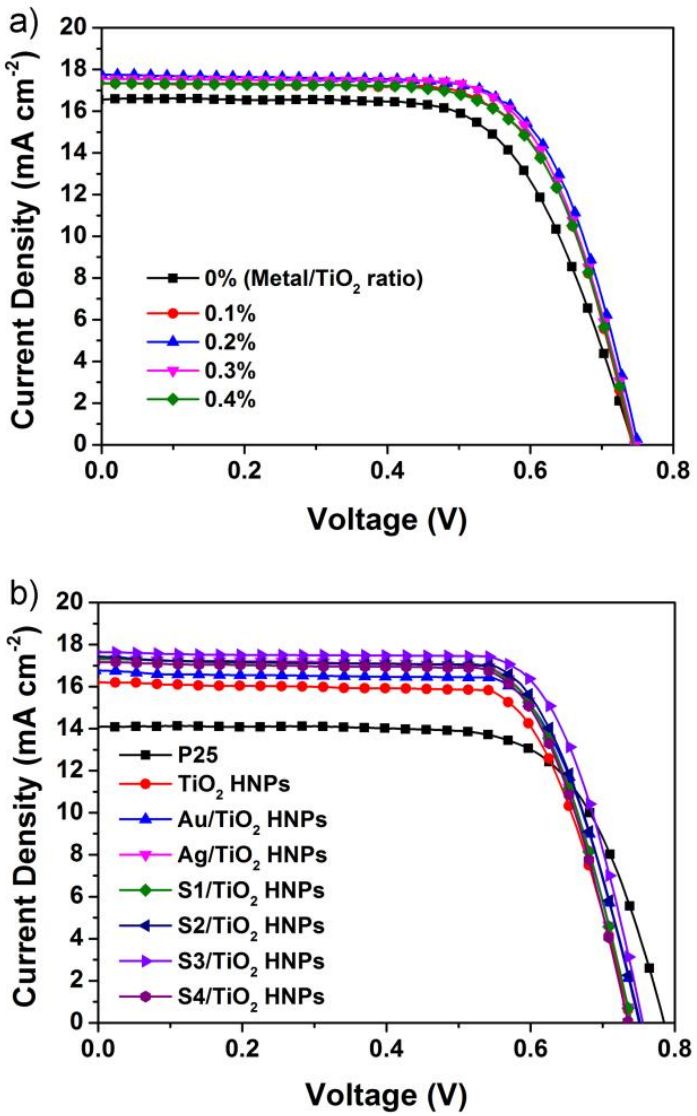

Figure 35. Current-voltage curve (*J-V* curve) of DSSCs based on a) TiO_2 HNPs with and without S3/TiO_2 HNPs with respect to metal amount and b) P25, TiO_2 HNPs and each samples with same amount of metal (0.2wt%).

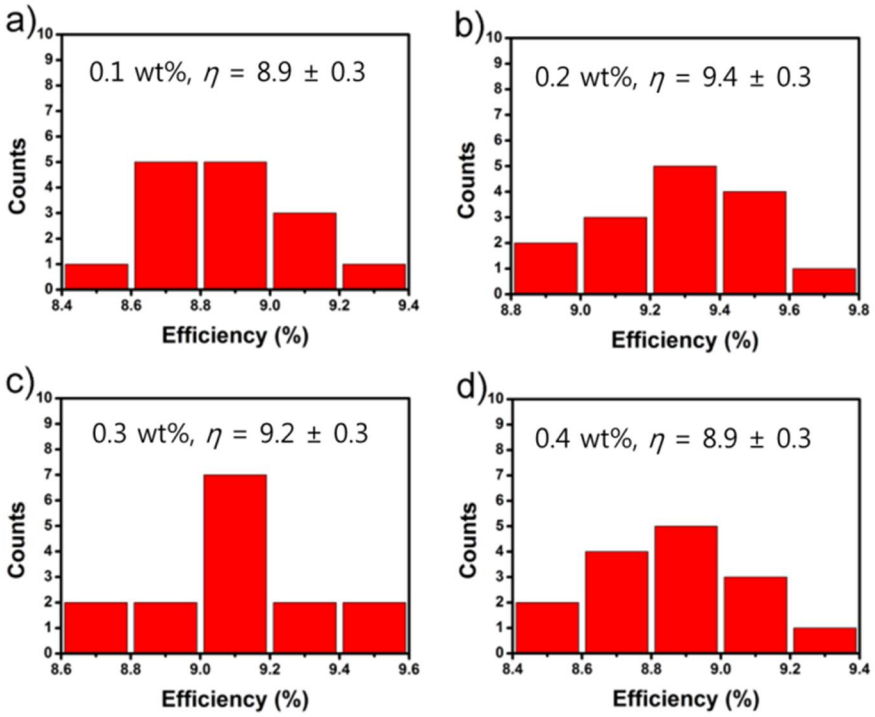

Figure 36. Histograms of power conversion efficiency for S3/TiO_2 HNPs based DSSCs with repect to metal amount. a) 0.1 wt%, b) 0.2 wt%, c) 0.3 wt%, d) 0.4 wt%, composed of 15 separate devices.

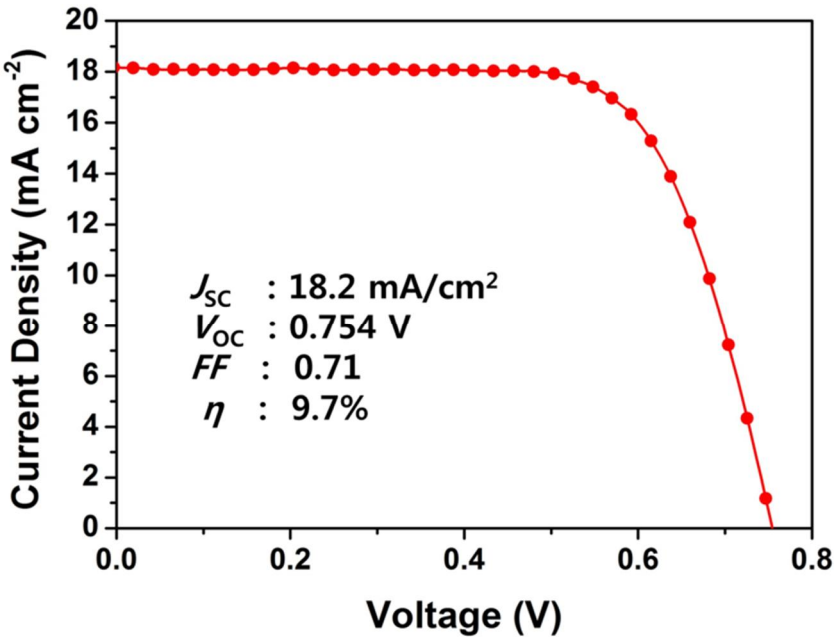

Figure 37. Current-voltage curve of best performing DSSCs based on S3/TiO_2 HNPs

Table 2. Photovoltaic parameter based on TiO_2 HNPs photoanodes with and without Au@Ag/TiO_2 HNPs coated with a SiO_2 layer.

Sample[a]	J_{sc}[b] (mA cm^{-2})	V_{oc}[c] (V)	FF[d]	η[e] (%)
P25	14.1	0.79	0.71	7.8
TiO_2 HNP	15.8	0.74	0.71	8.3
Au/TiO_2 HNP	16.3	0.75	0.72	8.8
Ag/TiO_2 HNP	16.8	0.75	0.71	9.0
S1/TiO_2 HNP	16.7	0.75	0.71	8.8
S2/TiO_2 HNP	16.9	0.75	0.72	9.1
S3/TiO_2 HNP	17.3	0.75	0.72	9.4
S4/TiO_2 HNP	16.8	0.75	0.71	9.0

[a] Active area of the assembled DSSC samples is 0.16 cm^2. [b] Short-circuit current. [c] Open-circuit voltage. [d] fill factor. [e] power conversion efficiency.

Table 3. Photovoltaic parameters of DSSCs with photoanodes containing S3/TiO_2 HNPs coated with a SiO_2 layer

Sample[a]	J_{sc}[b] (mA cm^{-2})	V_{oc}[c] (V)	FF[d]	η[e] (%)
TiO_2 HNP (0wt%)	16.6	0.74	0.66	8.2
0.1wt%	17.3	0.74	0.69	8.9
0.2wt%	17.7	0.75	0.7	9.3
0.3wt%	17.5	0.75	0.7	9.2
0.4wt%	17.3	0.75	0.69	8.9

[a] Active area of the assembled DSSC samples is 0.16 cm^2. [b] Short-circuit current. [c] Open-circuit voltage. [d] fill factor. [e] power conversion efficiency

3.3. Fabrication of monodisperse nitrogen-doped carbon double-shell hollow nanoparticles for supercapacitors

3.3.1. Fabrication of monodisperse nitrogen-doped carbon double-shell hollow nanoparticles

Figure 38 illustrates a schematic diagram of nitrogen-doped carbon double-shell hollow nanoparticle (NC DS-HNP) fabrication. The NC DS-HNPs were synthesized *via* a template method with polydopamine (PD) coating. The SiO_2/TiO_2 double-shell hollow nanoparticles (ST DS-HNPs) that were used as templates were synthesized *via* a sonication-mediated etching process, as previously reported.[112, 113] First, the SiO_2/TiO_2 core/shell NPs (ST CSNPs) were created using a sol-gel method. Polyvinylpyrrolidone (PVP) was then added to the ST CSNPs to form SiO_2 on the surface of TiO_2. The carbonyl groups of the PVP interacted with the hydroxyl groups of the oxide surfaces. The PVP-treated ST CSNPs were coated with SiO_2 shells *via* the Stöber method, which resulted in $SiO_2/TiO_2/SiO_2$ core/shell nanoparticles (STS CSNPs). The $SiO_2/TiO_2/SiO_2/TiO_2$ core/shell nanoparticles (STST CSNPs) were fabricated by repeating the steps. Finally, STST CSNPs were etched with an NH_4OH solution under sonication to obtain

ST DS-HNPs. The etched silica and titania were released into the solution and diffused from inside to the titania shell. The silica and titania species were condensed and re-deposited on the titania shell due to Ostwald ripening.[115] **Figure 39** exhibits TEM images of STST CSNPs, intermediate structured ST DS-HNP, and ST DS-HNPs as the etching proceeds. **Figure 40a** displays scanning transmission electron microscopy (STEM) images of ST DS-HNPs (average diameter: 220 nm). **Figure 40b–d** display elemental dot mapping images of ST DS-HNPs. These images confirmed that the ST DS-HNPs had inner and outer shells composed of silica and titania. The ST DS-HNPs used as templates were dispersed in deionized water. Then, the carbon precursor was deposited onto the inner and outer shells of the ST DS-HNPs template by PD pyrolysis. After carbonization of PD at 800°C, the templates were removed with dilute HF solution, leaving NC DS-HNPs.

Figure 41a and **b** exhibit TEM images of SiO_2/TiO_2 single-shell hollow nanoparticles (ST SS-HNP) and ST DS-HNPs templates; the average particle size was 220 nm. Carbonization and etching processes formed the nitrogen-doped carbon single-shell nanoparticles (NC SS-HNPs) and NC DS-HNPs. The NC SS-HNPs of the same size as the

NC DS-HNPs were used as a control to evaluate the effect of the number of shells. **Figure 41c** and **d** display TEM images of the NC SS-HNPs and NC DS-HNPs with an average diameter of 220 nm. Unlike the ST DS-HNPs, the inner shell of the NC DS-HNPs was not always located in the center of the NC DS-HNPs. It was usually moved to within the outer shell after elimination of the SiO_2/TiO_2 template. The TEM and FE-SEM images of a collection of NC DS-HNPs in **Figure 42a** and **Figure 43** confirmed the uniformity of the fabricated NC DS-HNPs.

Scanning transmission electron microscopy-energy dispersive spectroscopy (STEM-EDS) was used to investigate the elemental distribution in the NC DS-HNPs; the elemental dot maps and line analyses are shown in **Figure 44**. **Figure 44a** and **42b** display STEM and high-resolution TEM (HR-TEM) images of the NC DS-HNPs, revealing inner and outer shells with average diameters of 120 and 220 nm, respectively. The thicknesses of the inner and outer shells were about 20 and 30 nm, respectively. **Figures 44b–d** display elemental dot maps of the NC DS-HNPs. In **Figure 44b**, the overlapping elemental dot maps of the NC DS-HNPs are seen as red dots on the green shells, demonstrating that the well-defined DS-HNPs consisted of a relatively

large amount of carbon and a small amount of nitrogen. **Figure 44c and d** exhibit the carbon and nitrogen dot maps, respectively. The STEM-EDS line analysis shown in **Figure 44e** indicates that the NC DS-HNPs had inner and outer shells containing carbon and nitrogen, and that the elements were uniformly distributed. The atomic ratio of carbon to nitrogen was 0.05 according to STEM-EDS analyses, which indicated that nitrogen was doped in the carbon shells.

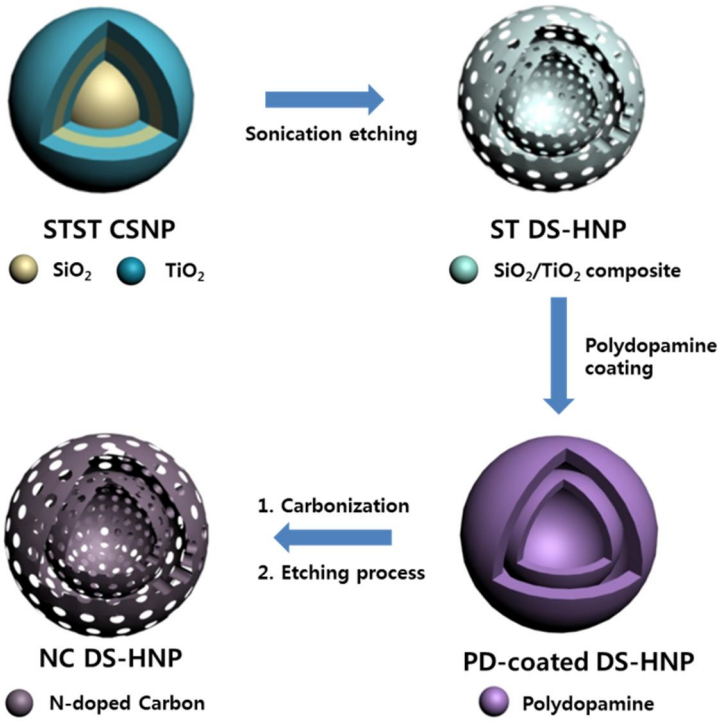

Figure 38. Schematic illustration of NC DS-HNP synthesis. NC DS-HNPs: nitrogen-doped carbon double-shell hollow nanoparticles; STST CSNPs: $SiO_2/TiO_2/SiO_2/TiO_2$ core/shell nanoparticles; ST DS-HNPs: SiO_2/TiO_2 double-shell hollow nanoparticles; PD: polydopamine.

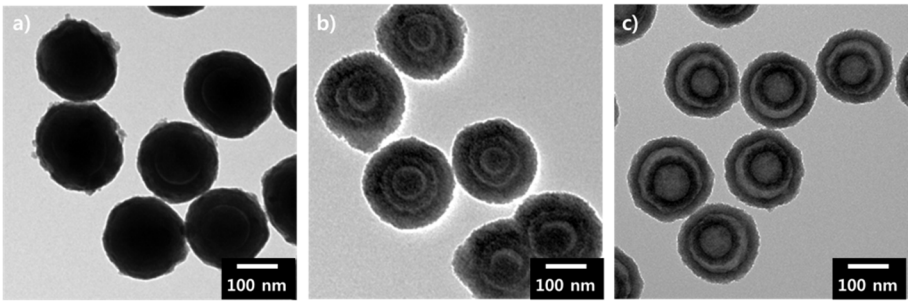

Figure 39. TEM images of a) STST CSNPs, b) intermediate structured ST DS-HNPs, and c) ST DS-HNPs

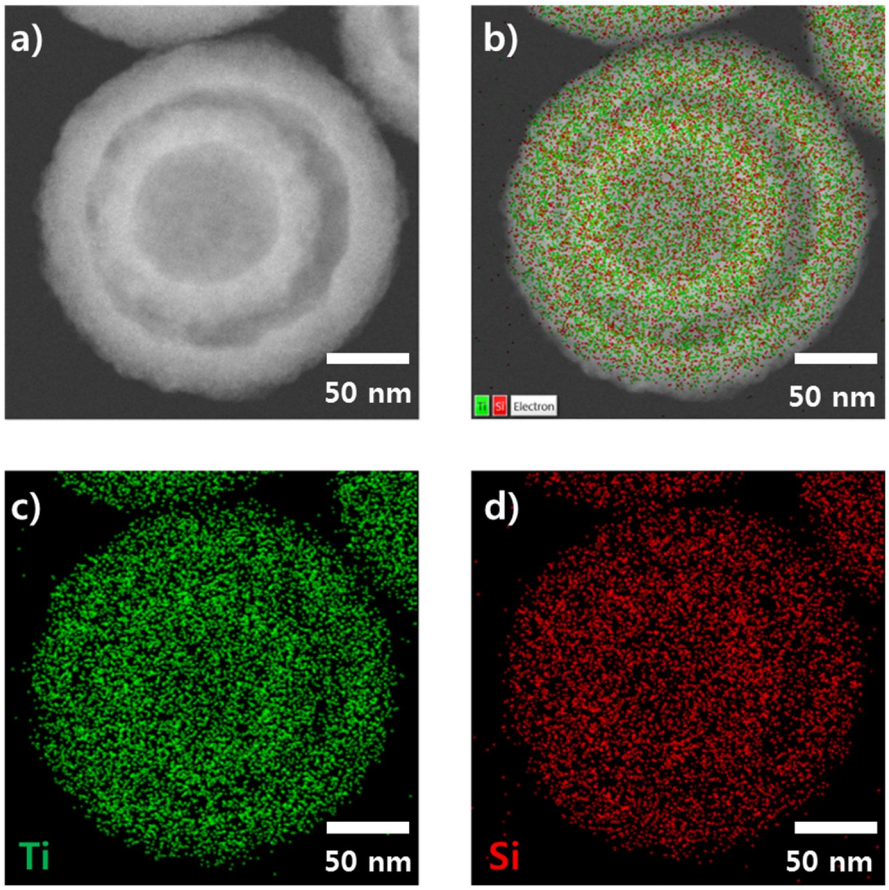

Figure 40. a) Scanning transmission electron microscopy (STEM) image of a silica/titania double-shell nanoparticle (ST DS-HNP) and the corresponding elemental dot maps for b) Ti and Si, c) Ti and d) Si.

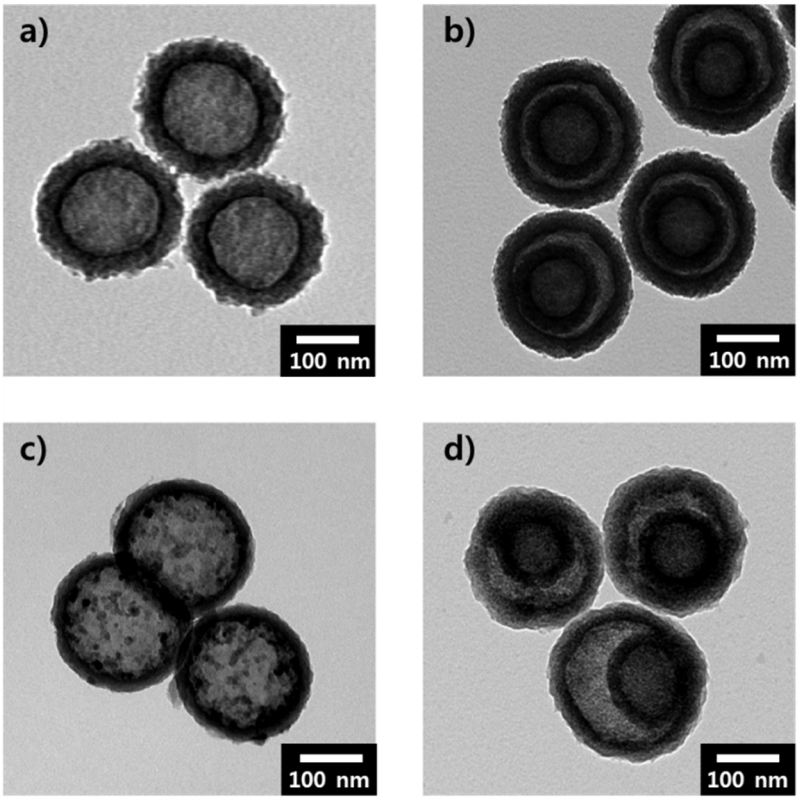

Figure 41. Transmission electron microscopy (TEM) images of a) ST SS-HNPs, b) ST DS-HNPs, c) NC SS-HNPs, and d) NC DS-HNPs.

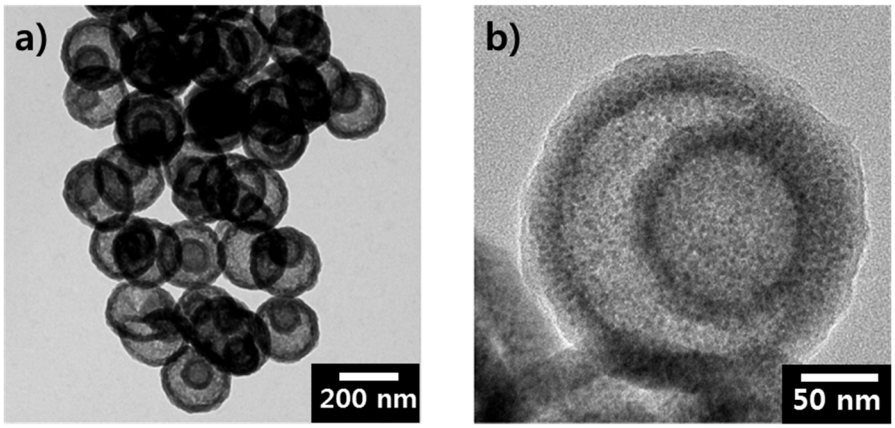

Figure 42. a) Transmission electron microscopy (TEM) image and b) high-resolution TEM (HR-TEM) image of nitrogen-doped carbon double-shell nanoparticles (NC DS-HNPs).

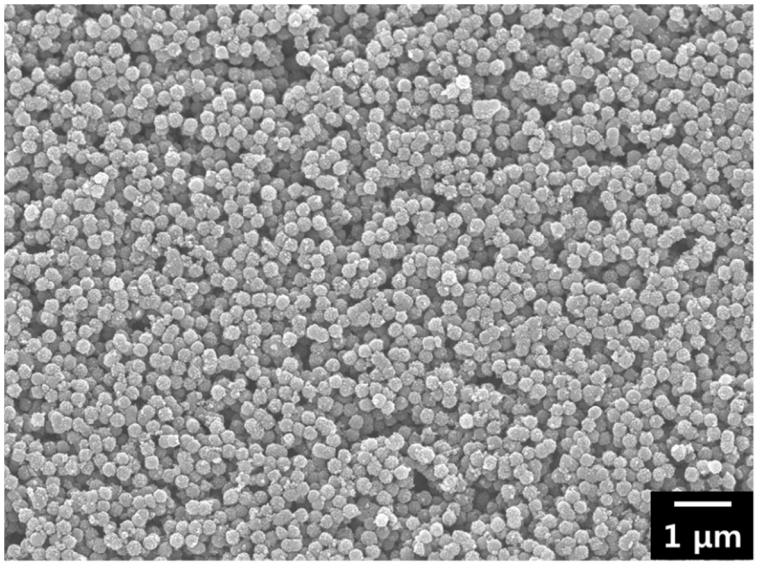

Figure 43. Low-magnification FE-SEM image of NC DS-HNPs

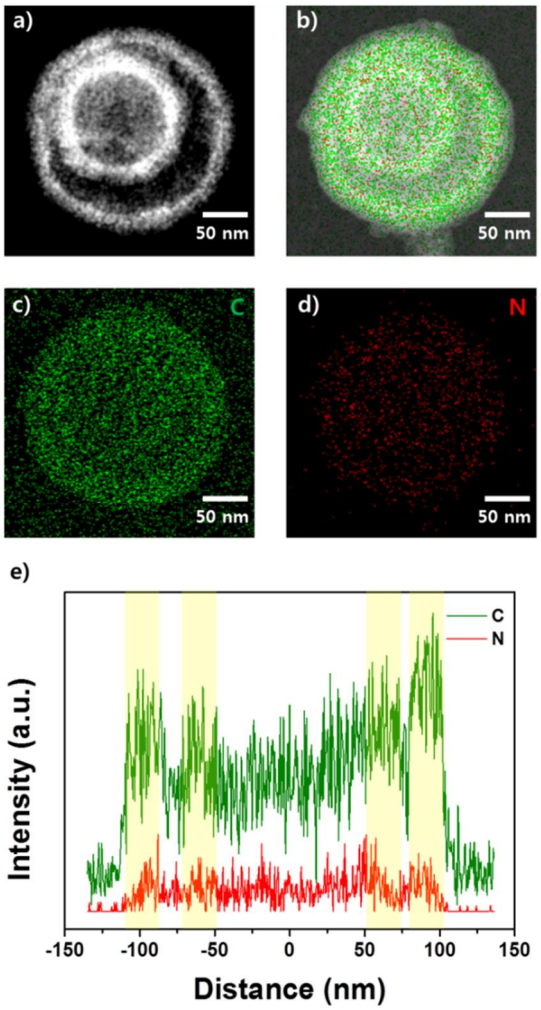

Figure 44. a) Scanning transmission electron microscopy (STEM) image of NC DS-HNPs and the corresponding b) overlapped elemental dot maps, c) carbon map and d) nitrogen map. e) STEM-energy dispersive spectroscopy (STEM-EDS) line maps of NC DS-HNPs. The green color represents carbon; the red color indicates nitrogen

3.3.2. Characterization of NC DS-HNPs

The Brunauer–Emmett–Teller (BET) analyses of the NC SS, DS-HNPs and their equivalent Barrett–Joyner–Halenda (BJH) pore size distributions were used to evaluate the pore characteristics. **Figure 45a** and **b** provide BET analyses of the NC SS-HNPs and NC DS-HNPs, respectively. Both had type-IV isotherms that indicated mesoporous characteristics and a large specific surface area.[142] Because the templates had mesoporous characteristics, nanopores in the nitrogen-doped carbon shell were generated during carbonization. From the pore characteristics in **Table 4**, the BET surface areas of the NC DS-HNPs and NC SS-HNPs were 873.52 and 511.21 $m^2\ g^{-1}$, and pore volume were 2.86 and 0.88 $cm^3\ g^{-1}$, respectively. This demonstrated that the inner shell of the NC DS-HNPs increased the BET surface area and pore volume. **Figure 45c** and **d** exhibit the BJH pore size distributions of the NC SS-HNPs and NC DS-HNPs, respectively. Both consisted of small (4.1 ± 0.5 nm) and large (≥ 20 nm) pores within the intrashell and inner cavities. The data indicate that the NC DS-HNPs had more small and large pores compared with the NC SS-HNPs, which resulted in a higher surface area and pore volume. The amount of large pores in the NC DS-HNPs was greater because the presence of the inner shell

provided more pores. The pores between the inner and outer shells and the inside pores of the inner shell increased the number of large pores.

X-ray photoelectron spectroscopy (XPS) was used to investigate the elemental chemical states and contents of the NC DS-HNPs. **Figure 46a** exhibits the survey spectra of the NC DS-HNPs, revealing the presence of C, O, and N. The carbon content in the NC DS-HNPs dominated; the atomic nitrogen concentration was 4.62%. This result was in good agreement with STEM-EDS observations. The presence of the O1s peak in the survey spectrum of the NC DS-HNPs was attributed to partial surface oxidation.[100, 143] **Figure 46b** displays the high-resolution C 1s peak, which was deconvoluted into four components. The peaks at 284.5, 285.3, 285.27, and 288.61 eV were assigned to C=C, C–C, C–O and C=N, and C–O–C and C–N functional groups, respectively.[143, 144] The C=C configuration was the main C 1s peak, and was responsible for the good electrical properties. The nitrogen-doped carbon structure also improved the electrochemical properties.[145] The high-resolution N 1s peak was deconvoluted into the following four components: pyridinic N (398.22), pyrrolic or pyridonic N (399.47), quaternary N (400.74), and oxidized N (402.02 eV) as shown in **Figure 46c**. [146, 147] The pyridinic and quaternary

nitrogens comprised large portions of the N 1s peak; these groups are more electrocatalytically active than the others.[148] The pyridinic N atoms were located at the edge of the carbon plane, and the quaternary N atoms were bonded to three carbon atoms within the carbon plane. The nitrogen functional groups provide chemically active sites to improve the electrochemical properties of supercapacitors. Hence, carbonization of PD would be a good approach to introduce chemically active sites into carbon materials

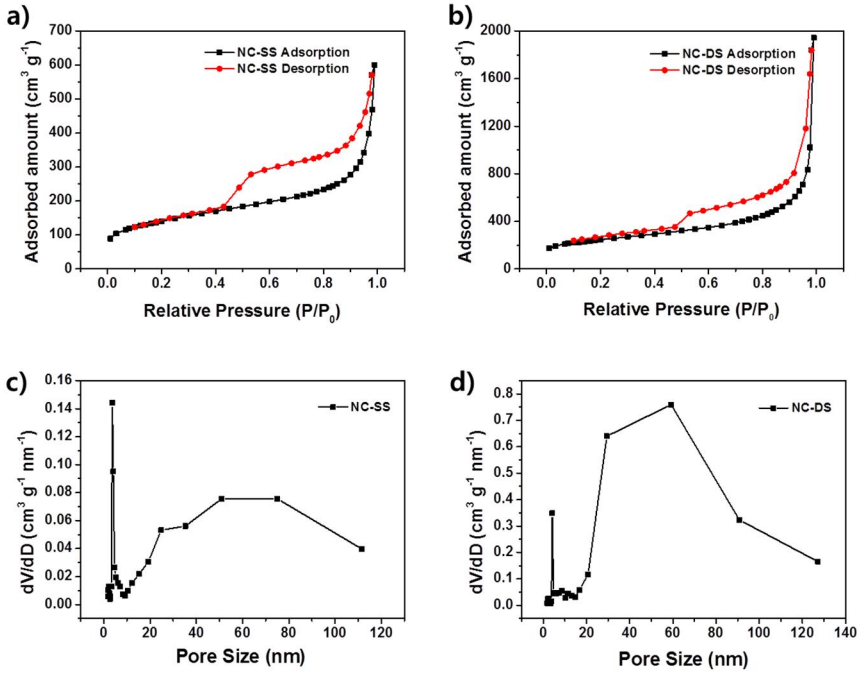

Figure 45. Brunauer–Emmett–Teller (BET) analyses of a) NC SS-HNPs and b) NC DS-HNPs. Barrett–Joyner–Halenda (BJH) pore size distributions of c) NC SS-HNPs and d) NC DS-HNPs

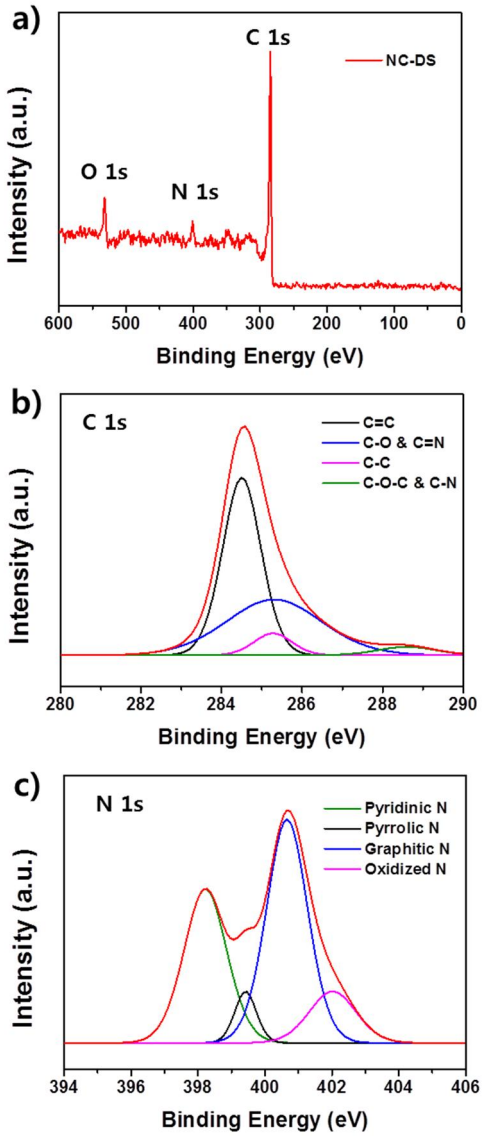

Figure 46. a) X-ray photoelectron spectra (XPS) of the NC DS-HNPs and the corresponding high-resolution XPS spectra of b) C 1s and c) N 1s features.

Table 4. Pore characteristics of NC SS-HNPs and NC DS-HNPs.

Sample	S_{BET} ($m^2\ g^{-1}$)	$S_{Langmuir}$ ($m^2\ g^{-1}$)	V_{pore} ($cm^3\ g^{-1}$)	D_{ave} (nm)
NC SS-HNPs	511.21	702.83	0.88	7.4
NC DS-HNPs	873.52	1198.77	2.86	13.9

3.3.3. Electrochemical performance of NC DS-HNPs based supercapapcitors

To further investigate properties of NC DS-HNPs, the electrochemical performance of the NC DS-HNPs was measured by cyclic voltammetry and galvanostatic charge–discharge tests in a three-electrode cell in 1M H_2SO_4 solution. **Figure 47a** compares the cyclic voltammetry (CV) curve of NC SS-HNPs and NC DS-HNPs based supercapacitors at 20 mV s^{-1}. Both curve exhibit quasi-rectangular shapes with pseudo capacitance behavior. The NC DS-HNPs based supercapacitor has a larger curve, indicating a higher capacitance due to high surface area and pore volume. The galvanostatic charge-discharge curve also reflects higher capacitance of the NC DS-HNPs based supercapacitor than the NC SS-HNPs. (**Figure 47b**) The pseudo-capacitive behavior over a wide voltage was attributed to a Faradaic redox reaction of the nitrogen dopants.[149] Nitrogen doping in carbon materials improve supercapacitive performance *via* participation in a pseudo-capacitance reaction enabled by enhanced electrolyte wettability and electrical conductivity.[150, 151] To investigate electrolyte wettability of nitrogen doped carbon, the water contact angle of carbon based films were measured. (**Figure 48**) The control of NC DS-HNPs film was

carbon black film which had no heteroatom. The contact angle of NC DS-HNPs film was smaller than that of carbon black film. This result indicated the nitrogen doping increased the electrolyte wettability. Furthermore, the porous nanostructures and high surface area of the hollow structure also enhances supercapacitive performance. The nanopores in the nitrogen-doped carbon double-shell allow greater absorption of electrolyte ions, increasing the capacitance. **Figure 49a** displays CV curves of NC DS-HNPs based supercapacitor with different scan rates. The CV curves retained quasi-rectangular shape from 5 to 100 mV s^{-1}, revealing good rate electrochemical performance. **Figure 49b** exhibits the galvanostatic charge–discharge curves of the NC DS-HNPs; the nonlinearity indicates pseudo-capacitive behavior.[100] The specific capacitance approached 202 F g^{-1} at a current density of 0.5 A g^{-1}, and the capacitance retention was 75% in 1M H_2SO_4 solution at a current density ranging from 0.5 to 10 A g^{-1}. Excellent retention is important for applications with a high discharge–recharge rate. **Table 5** displays the capacitance of N-doped carbon materials reported in literatures. The NC DS-HNPs based supercapacitor had relatively high capacitance. **Figure 49c** shows the electrochemical impedance spectroscopy (EIS) results over a frequency

ranging from 0.01 Hz to 0.1 MHz; the inset presents the high-frequency data. The Nyquist plot was semicircular at high frequencies and a straight line at low frequencies. The intercept at the start of the semicircle and the size of the semicircle correspond to the series resistance and the charge transfer resistance at the interface between the electrode and electrolyte, which were 1.1 and 1.45 Ω, respectively. The small resistances indicated favorable charge-transfer kinetics for the NC DS-HNPs electrode. **Figure 49d** indicates that NC SS-HNPs and NC DS-HNPs based electrodes were electrochemically stable with only 9 % and 7 % loss in specific capacitance after 5000 cycles at a current density of 1 A g^{-1}, respectively. The NC DS-HNPs based electrode was more stable than the NC SS-HNPs based one. The excellent capacitance retention indicated a robust structure over the charge–discharge process. **Figure 50** exhibits the robust structure of NC DS-HNPs after 5000 cycles at a current density of 1 A g^{-1}. The NC DS-HNPs had a unique structure and composition, which led to high specific capacitance, outstanding stability, and remarkable capacitance retention.

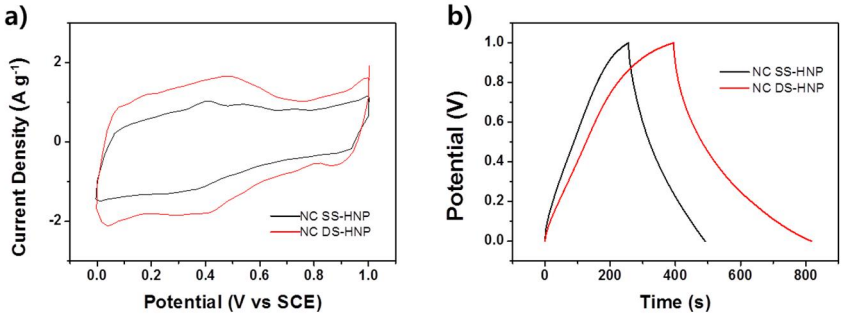

Figure 47. a) CV curves of NC SS-HNP and NC DS-HNP at a scan rate 20 mV s^{-1} in 1M H_2SO_4 solution and b) charge-discharge curves of NC SS-HNP and NC DS-HNP at current density of 0.5 A g^{-1}.

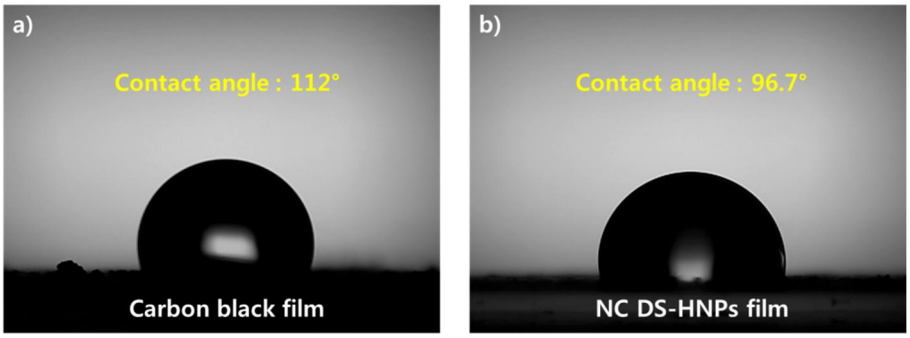

Figure 48. Water contact angle of a) carbon black film and b) NC DS-HNPs film.

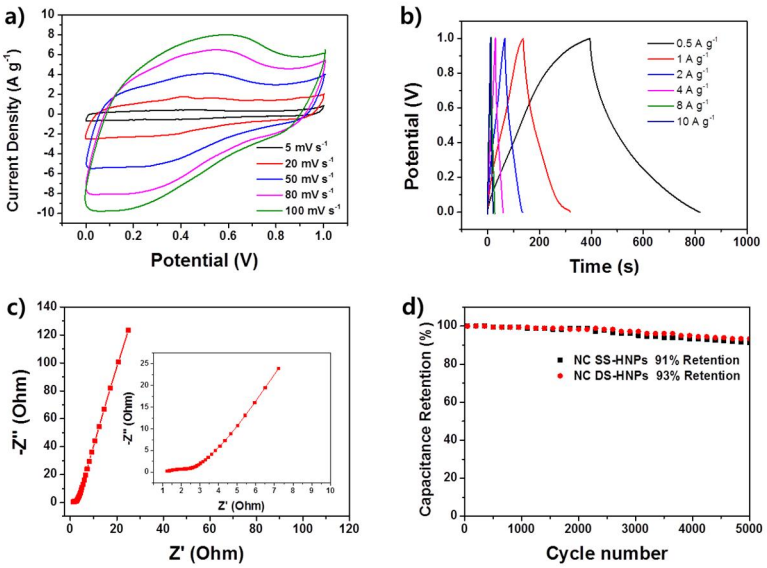

Figure 49. a) Cyclic voltammograms of the NC DS-HNPs at various scan rates, b) charge–discharge curves of the NC DS-HNPs, c) electrochemical impedance spectra (EIS) of the NC DS-HNPs (inset: magnified region), and d) cycling performance of the NC SS-HNPs and NC DS-HNPs at a current density of 1 A g^{-1}.

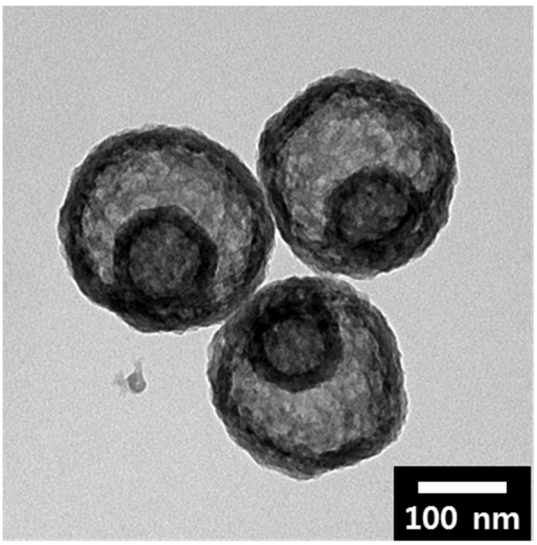

Figure 50. TEM image of NC DS-HNPs after 5000 cycles at a current density of 1 A g^{-1}

Table 5. Capacitances of N-doped carbon materials from the literature

Sample	Capacitance (F g^{-1})	Current density (A g^{-1})	Electrolyte	Ref
Porous N-doped hollow carbon sphere	176	1	6M KOH	[152]
N-doped mesoporous carbon	180	1	1M H_2SO_4	[153]
N-doped porous carbon	210	1	6M KOH	[154]
Mesoporous N-doped carbons	182	1	6M KOH	[155]
N-doped hollow carbon sphere	170	1	6M KOH	[156]
NC DS-HNPs	184	1	1M H_2SO_4	This work

4. Conclusion

The various inorganic hollow nanostructures (Au@Ag/TiO_2 HNPs, SiO_2/TiO_2 based HNPs, NC DS-HNPs) were successfully fabricated by sol-gel and hard template. Furthermore, as-prepared materials displayed promising properties in the energy-related application. The subtopic is concluded in the view point of each subtopic as follows:

1. Two types of HNP as a scaffold layer and an Al-TiO_2 compact layer were introduced into PSCs to improve efficiency. STHNPs included amorphous phases of SiO_2 and TiO_2, while THNPs included a crystalline TiO_2 anatase phase. Both HNPs improved perovskite loading, leading to increased J_{sc}. Unlike THNPs, STHNPs acted as insulators in the scaffold layer, leading to enhanced V_{oc}. In addition, Al doping of the compact layer at low temperature ($\leq$150 °C) led to an increase in J_{sc} and V_{oc} due to easy electron extraction and a reduced recombination rate. Overall, implementation of STHNP scaffold layers and Al-TiO_2 compact layers led to a higher PCE of 14.7%, compared to 10.7% for PSCs based on silica NPs with a TiO_2 compact layer.

2. The Au@Ag/TiO_2 HNPs were successfully fabricated *via* sol-gel coating and chemical deposition. The Au@Ag CSNPs exhibited

stronger and broader surface plasmon resonance than either the Au or Ag nanoparticles. By varying the thickness of the Ag shell, the LSPR could be controlled, and to investigate the interaction between the Au core and Ag shell. TiO_2 HNPs with a larger specific surface area provide sufficient dye loading and effective optical scattering, leading to increased PCE compared with using P25 nanoparticles. The overall PCE of η = 9.7% was achieved by incorporating the Au@Ag/TiO_2 HNPs into the photoanode material for the DSSCs, which is a significant improvement compared with DSSCs formed using P25 (η = 7.8%). The approach described here enables the fabrication of novel structured Au@Ag/TiO_2 HNPs with a large specific surface area, large optical scattering effect, and tuned LSPR. The applications of these nanoparticles extend beyond DSSCs to include photocatalysis, perovskite solar cells, organic solar cells, and antimicrobial therapy.

3. A uniquely structured NC DS-HNPs were fabricated using a straightforward approach. These nanoparticles were fabricated *via* polymerization of dopamine onto ST DS-HNPs, followed by carbonization and etching. The morphology of the nitrogen-doped carbon was decided by controlling the number of template shells. The incorporation of nitrogen led to increased electrolyte wettability, good

electrical conductivity and pseudo-capacitance. The high surface area of the NC DS-HNPs resulted in a high specific capacitance of 202 F g^{-1} at current density of 0.5 A g^{-1}. The robust structure of an NC DS-HNPs electrode enabled good cyclic stability (93% capacitance retention after 5,000 cycles). This technique of fabricating well-defined carbon hollow structures will assist in the development of other novel porous materials.

References

[1] Y. Wang, N. Herron, The Journal of Physical Chemistry, **1991**, 95, 525.

[2] A.P. Alivisatos, Science, **1996**, 271, 933.

[3] N. Félidj, J. Aubard, G. Lévi, J.R. Krenn, A. Hohenau, G. Schider, A. Leitner, F.R. Aussenegg, Appl. Phys. Lett., **2003**, 82, 3095.

[4] E. Roduner, Chem. Soc. Rev., **2006**, 35, 583.

[5] K. Koga, T. Ikeshoji, K.-i. Sugawara, Phys. Rev. Lett., **2004**, 92, 115507.

[6] D.L. Leslie-Pelecky, R.D. Rieke, Chem. Mater., **1996**, 8, 1770.

[7] D. Cahen, G. Hodes, M. Grätzel, J.F. Guillemoles, I. Riess, The Journal of Physical Chemistry B, **2000**, 104, 2053.

[8] N. Robertson, Angewandte Chemie International Edition, **2006**, 45, 2338.

[9] G. Wang, L. Zhang, J. Zhang, Chem. Soc. Rev., **2012**, 41, 797.

[10] M. Yang, J. Ma, C. Zhang, Z. Yang, Y. Lu, Angewandte Chemie International Edition, **2005**, 44, 6727.

[11] L. Vayssieres, Adv. Mater., **2003**, 15, 464.

[12] A.E. Danks, S.R. Hall, Z. Schnepp, Materials Horizons, **2016**, 3, 91.

[13] G. Korotcenkov, B. Cho, Metal oxide composites in conductometric gas sensors: Achievements and challenges, 2016.

[14] R.A. Caruso, M. Antonietti, Chem. Mater., **2001**, 13, 3272.

[15] M. Nieuwland, P. Geerdink, P. Brier, P. van den Eijnden, J.T.M.M. Henket, M.L.P. Langelaan, N. Stroeks, H.C. van Deventer, A.H. Martin, Innovative Food Science & Emerging Technologies, **2013**, 20, 269.

[16] Z. Feng, Y. Li, D. Niu, L. Li, W. Zhao, H. Chen, L. Li, J. Gao, M.

Ruan, J. Shi, Chem. Commun., **2008**, 2629.
[17] W. Zhao, M. Lang, Y. Li, L. Li, J. Shi, J. Mater. Chem., **2009**, 19, 2778.
[18] X.W. Lou, L.A. Archer, Z. Yang, Adv. Mater., **2008**, 20, 3987.
[19] Y. Sun, Y. Xia, J. Am. Chem. Soc., **2004**, 126, 3892.
[20] Q. Zhang, T. Zhang, J. Ge, Y. Yin, Nano Lett., **2008**, 8, 2867.
[21] S.-H. Wu, C.-Y. Mou, H.-P. Lin, Chem. Soc. Rev., **2013**, 42, 3862.
[22] Y. Xu, Z. Lin, X. Zhong, X. Huang, N.O. Weiss, Y. Huang, X. Duan, Nat Commun, **2014**, 5.
[23] J. Jun, J.S. Lee, D.H. Shin, S.G. Kim, J. Jang, Nanoscale, **2015**, 7, 16026.
[24] C. Choi, J.A. Lee, A.Y. Choi, Y.T. Kim, X. Lepró, M.D. Lima, R.H. Baughman, S.J. Kim, Adv. Mater., **2014**, 26, 2059.
[25] M. Liu, J. Qian, Y. Zhao, D. Zhu, L. Gan, L. Chen, J. Mater. Chem. A, **2015**, 3, 11517.
[26] J. Lee, J. Kim, T. Hyeon, Adv. Mater., **2006**, 18, 2073.
[27] F. Xu, Z. Tang, S. Huang, L. Chen, Y. Liang, W. Mai, H. Zhong, R. Fu, D. Wu, Nat Commun, **2015**, 6.
[28] A. Stein, Z. Wang, M.A. Fierke, Adv. Mater., **2009**, 21, 265.
[29] R. Liu, S.M. Mahurin, C. Li, R.R. Unocic, J.C. Idrobo, H. Gao, S.J. Pennycook, S. Dai, Angewandte Chemie International Edition, **2011**, 50, 6799.
[30] G. Zheng, S.W. Lee, Z. Liang, H.-W. Lee, K. Yan, H. Yao, H. Wang, W. Li, S. Chu, Y. Cui, Nat Nano, **2014**, 9, 618.
[31] S.L. Candelaria, Y. Shao, W. Zhou, X. Li, J. Xiao, J.-G. Zhang, Y. Wang, J. Liu, J. Li, G. Cao, Nano Energy, **2012**, 1, 195.
[32] S.B. Yoon, K. Sohn, J.Y. Kim, C.H. Shin, J.S. Yu, T. Hyeon, Adv. Mater., **2002**, 14, 19.
[33] J.-S. Yu, S. Kang, S.B. Yoon, G. Chai, J. Am. Chem. Soc., **2002**,

124, 9382.
[34] S. Yang, X. Feng, L. Zhi, Q. Cao, J. Maier, K. Müllen, Adv. Mater., **2010**, 22, 838.
[35] R.J. White, K. Tauer, M. Antonietti, M.-M. Titirici, J. Am. Chem. Soc., **2010**, 132, 17360.
[36] A.-H. Lu, T. Sun, W.-C. Li, Q. Sun, F. Han, D.-H. Liu, Y. Guo, Angewandte Chemie International Edition, **2011**, 50, 11765.
[37] J. Hammond, N. Bhalla, S. Rafiee, P. Estrela, Localized Surface Plasmon Resonance as a Biosensing Platform for Developing Countries, 2014.
[38] H. Choi, W.T. Chen, P.V. Kamat, ACS Nano, **2012**, 6, 4418.
[39] S.D. Standridge, G.C. Schatz, J.T. Hupp, Langmuir, **2009**, 25, 2596.
[40] M. Banerjee, S. Sharma, A. Chattopadhyay, S.S. Ghosh, Nanoscale, **2011**, 3, 5120.
[41] J.E. Millstone, G.S. Métraux, C.A. Mirkin, Adv. Funct. Mater., **2006**, 16, 1209.
[42] W. Niu, S. Zheng, D. Wang, X. Liu, H. Li, S. Han, J. Chen, Z. Tang, G. Xu, J. Am. Chem. Soc., **2009**, 131, 697.
[43] L. Chuntonov, M. Bar-Sadan, L. Houben, G. Haran, Nano Lett., **2012**, 12, 145.
[44] C.M. Gonzalez, Y. Liu, J.C. Scaiano, J. Phys. Chem. C, **2009**, 113, 11861.
[45] X. Zhang, Z. Su, Adv. Mater., **2012**, 24, 4574.
[46] D.B. Mitzi, S. Wang, C.A. Feild, C.A. Chess, A.M. Guloy, Science, **1995**, 267, 1473.
[47] H.S. Kim, C.R. Lee, J.H. Im, K.B. Lee, T. Moehl, A. Marchioro, S.J. Moon, R. Humphry-Baker, J.H. Yum, J.E. Moser, M. Grätzel, N.G. Park, Scientific Reports, **2012**, 2.
[48] A. Kojima, K. Teshima, Y. Shirai, T. Miyasaka, J. Am. Chem.

Soc., **2009**, 131, 6050.
[49] J.H. Im, C.R. Lee, J.W. Lee, S.W. Park, N.G. Park, Nanoscale, **2011**, 3, 4088.
[50] W.S. Yang, J.H. Noh, N.J. Jeon, Y.C. Kim, S. Ryu, J. Seo, S.I. Seok, Science, **2015**, 348, 1234.
[51] C.S. Ponseca, T.J. Savenije, M. Abdellah, K. Zheng, A. Yartsev, T. Pascher, T. Harlang, P. Chabera, T. Pullerits, A. Stepanov, J.P. Wolf, V. Sundström, J. Am. Chem. Soc., **2014**, 136, 5189.
[52] S.D. Stranks, G.E. Eperon, G. Grancini, C. Menelaou, M.J.P. Alcocer, T. Leijtens, L.M. Herz, A. Petrozza, H.J. Snaith, Science, **2013**, 342, 341.
[53] G. Xing, N. Mathews, S. Sun, S.S. Lim, Y.M. Lam, M. Graẗzel, S. Mhaisalkar, T.C. Sum, Science, **2013**, 342, 344.
[54] M. Grätzel, Nat. Mater., **2014**, 13, 838.
[55] M. Liu, M.B. Johnston, H.J. Snaith, Nature, **2013**, 501, 395.
[56] J. Burschka, N. Pellet, S.J. Moon, R. Humphry-Baker, P. Gao, M.K. Nazeeruddin, M. Grätzel, Nature, **2013**, 499, 316.
[57] H. Zhou, Q. Chen, G. Li, S. Luo, T.B. Song, H.S. Duan, Z. Hong, J. You, Y. Liu, Y. Yang, Science, **2014**, 345, 542.
[58] N. Ahn, D.Y. Son, I.H. Jang, S.M. Kang, M. Choi, N.G. Park, J. Am. Chem. Soc., **2015**, 137, 8696.
[59] N.J. Jeon, J.H. Noh, Y.C. Kim, W.S. Yang, S. Ryu, S.I. Seok, Nat. Mater., **2014**, 13, 897.
[60] Y. Yu, J. Li, D. Geng, J. Wang, L. Zhang, T.L. Andrew, M.S. Arnold, X. Wang, ACS Nano, **2015**, 9, 564.
[61] J. Zhang, P. Barboux, T. Pauporté, Advanced Energy Materials, **2014**, 4.
[62] M.H. Kumar, N. Yantara, S. Dharani, M. Graetzel, S. Mhaisalkar, P.P. Boix, N. Mathews, Chem. Commun., **2013**, 49, 11089.
[63] D. Bi, G. Boschloo, S. Schwarzmüller, L. Yang, E.M.J.

Johansson, A. Hagfeldt, Nanoscale, **2013**, 5, 11686.
[64] D. Liu, T.L. Kelly, Nat. Photonics, **2014**, 8, 133.
[65] E.J. Juarez-Perez, M. Wußler, F. Fabregat-Santiago, K. Lakus-Wollny, E. Mankel, T. Mayer, W. Jaegermann, I. Mora-Sero, Journal of Physical Chemistry Letters, **2014**, 5, 680.
[66] J.T.W. Wang, J.M. Ball, E.M. Barea, A. Abate, J.A. Alexander-Webber, J. Huang, M. Saliba, I. Mora-Sero, J. Bisquert, H.J. Snaith, R.J. Nicholas, Nano Lett., **2014**, 14, 724.
[67] Q. Hu, J. Wu, C. Jiang, T. Liu, X. Que, R. Zhu, Q. Gong, ACS Nano, **2014**, 8, 10161.
[68] H.-S. Kim, N.-G. Park, The Journal of Physical Chemistry Letters, **2014**, 5, 2927.
[69] E.L. Unger, E.T. Hoke, C.D. Bailie, W.H. Nguyen, A.R. Bowring, T. Heumuller, M.G. Christoforo, M.D. McGehee, Energy & Environmental Science, **2014**, 7, 3690.
[70] M. Hadadian, J.-P. Correa-Baena, E.K. Goharshadi, A. Ummadisingu, J.-Y. Seo, J. Luo, S. Gholipour, S.M. Zakeeruddin, M. Saliba, A. Abate, M. Grätzel, A. Hagfeldt, Adv. Mater., **2016**, 28, 8681.
[71] Y. Zhang, L. Tan, Q. Fu, L. Chen, T. Ji, X. Hu, Y. Chen, Chem. Commun., **2016**, 52, 5674.
[72] K.M. Boopathi, R. Mohan, T.-Y. Huang, W. Budiawan, M.-Y. Lin, C.-H. Lee, K.-C. Ho, C.-W. Chu, J. Mater. Chem. A, **2016**, 4, 1591.
[73] F. Wang, H. Yu, H. Xu, N. Zhao, Adv. Funct. Mater., **2015**, 25, 1120.
[74] P.-W. Liang, C.-Y. Liao, C.-C. Chueh, F. Zuo, S.T. Williams, X.-K. Xin, J. Lin, A.K.Y. Jen, Adv. Mater., **2014**, 26, 3748.
[75] C. Zuo, L. Ding, Nanoscale, **2014**, 6, 9935.
[76] Y. Guo, K. Shoyama, W. Sato, E. Nakamura, Advanced Energy

Materials, **2016**, 6, 1502317.
[77] G. Yang, H. Tao, P. Qin, W. Ke, G. Fang, J. Mater. Chem. A, **2016**, 4, 3970.
[78] S. Yang, W. Fu, Z. Zhang, H. Chen, C.-Z. Li, J. Mater. Chem. A, **2017**, 5, 11462.
[79] B. O'Regan, M. Grätzel, Nature, **1991**, 353, 737.
[80] M. Grätzel, Nature, **2001**, 414, 338.
[81] A. Hagfeldt, G. Boschloo, L. Sun, L. Kloo, H. Pettersson, Chem. Rev., **2010**, 110, 6595.
[82] B. Mphande, A. Pogrebnoi, Outdoor Photoelectrochemical Characterization of Dyes from Acalypha wilkesiana 'Haleakala' and Hibiscus sabdariffa as Dye Solar Cells Sensitizers, 2015.
[83] A. Yella, H.W. Lee, H.N. Tsao, C. Yi, A.K. Chandiran, M.K. Nazeeruddin, E.W.G. Diau, C.Y. Yeh, S.M. Zakeeruddin, M. Grätzel, Science, **2011**, 334, 629.
[84] A.K. Chandiran, P. Comte, R. Humphry-Baker, F. Kessler, C. Yi, M.K. Nazeeruddin, M. Grätzel, Adv. Funct. Mater., **2013**, 23, 2775.
[85] S.D. Standridge, G.C. Schatz, J.T. Hupp, J. Am. Chem. Soc., **2009**, 131, 8407.
[86] N.C. Jeong, C. Prasittichai, J.T. Hupp, Langmuir, **2011**, 27, 14609.
[87] M.D. Brown, T. Suteewong, R.S.S. Kumar, V. D'Innocenzo, A. Petrozza, M.M. Lee, U. Wiesner, H.J. Snaith, Nano Lett., **2011**, 11, 438.
[88] S. Rühle, M. Shalom, A. Zaban, ChemPhysChem, **2010**, 11, 2290.
[89] E. Lee, J. Ryu, J. Jang, Chem. Commun., **2013**, 49, 9995.
[90] N.C. Jeong, O.K. Farha, J.T. Hupp, Langmuir, **2011**, 27, 1996.
[91] N.C. Jeong, H.J. Son, C. Prasittichai, C.Y. Lee, R.A. Jensen, O.K. Farha, J.T. Hupp, J. Am. Chem. Soc., **2012**, 134, 19820.
[92] S. Son, S.H. Hwang, C. Kim, J.Y. Yun, J. Jang, ACS. Appl.

Mater. Inter., **2013**, 5, 4815.
[93] S. Hore, C. Vetter, R. Kern, H. Smit, A. Hinsch, Sol. Energy Mater. Sol. Cells, **2006**, 90, 1176.
[94] J. Ferber, J. Luther, Sol. Energy Mater. Sol. Cells, **1998**, 54, 265.
[95] M. Law, L.E. Greene, J.C. Johnson, R. Saykally, P. Yang, Nat. Mater., **2005**, 4, 455.
[96] K. Shankar, J.I. Basham, N.K. Allam, O.K. Varghese, G.K. Mor, X. Feng, M. Paulose, J.A. Seabold, K.S. Choi, C.A. Grimes, J. Phys. Chem. C, **2009**, 113, 6327.
[97] G.K. Mor, K. Shankar, M. Paulose, O.K. Varghese, C.A. Grimes, Nano Lett., **2006**, 6, 215.
[98] P. Brown, K. Takechi, P.V. Kamat, J. Phys. Chem. C, **2008**, 112, 4776.
[99] Y.B. Tang, C.S. Lee, J. Xu, Z.T. Liu, Z.H. Chen, Z. He, Y.L. Cao, G. Yuan, H. Song, L. Chen, L. Luo, H.M. Cheng, W.J. Zhang, I. Bello, S.T. Lee, ACS Nano, **2010**, 4, 3482.
[100] J. Zhou, J. Lian, L. Hou, J. Zhang, H. Gou, M. Xia, Y. Zhao, T.A. Strobel, L. Tao, F. Gao, Nat Commun, **2015**, 6.
[101] L. Li, A.-R.O. Raji, J.M. Tour, Adv. Mater., **2013**, 25, 6298.
[102] X.-Y. Shan, Y. Wang, D.-W. Wang, F. Li, H.-M. Cheng, Advanced Energy Materials, **2016**, 6, n/a.
[103] H. Ji, X. Zhao, Z. Qiao, J. Jung, Y. Zhu, Y. Lu, L.L. Zhang, A.H. MacDonald, R.S. Ruoff, Nat Commun, **2014**, 5.
[104] J. Yun, J. Ryu, J. Lee, H. Yu, J. Jang, J. Mater. Chem. A, **2016**, 4, 1306.
[105] W. Zhou, X. Xiao, M. Cai, L. Yang, Nano Lett., **2014**, 14, 5250.
[106] Z. Wen, Q. Wang, Q. Zhang, J. Li, Electrochem. Commun., **2007**, 9, 1867.
[107] J. Noh, C.M. Yoon, Y.K. Kim, J. Jang, Carbon, **2017**, 116, 470.
[108] B.G. Choi, M. Yang, W.H. Hong, J.W. Choi, Y.S. Huh, ACS

Nano, **2012**, 6, 4020.
[109] A. González, E. Goikolea, J.A. Barrena, R. Mysyk, Renewable and Sustainable Energy Reviews, **2016**, 58, 1189.
[110] H.-Y. Wang, F.-X. Xiao, L. Yu, B. Liu, X.W. Lou, Small, **2014**, 10, 3181.
[111] S.H. Hwang, D.H. Shin, J. Yun, C. Kim, M. Choi, J. Jang, Chem.-Eur. J., **2014**, 20, 4439.
[112] J. Lee, S.H. Hwang, J. Yun, J. Jang, ACS Applied Materials & Interfaces, **2014**, 6, 15420.
[113] S. Lee, J. Lee, S.H. Hwang, J. Yun, J. Jang, ACS Nano, **2015**, 9, 4939.
[114] J. Yun, S.H. Hwang, J. Jang, ACS. Appl. Mater. Inter., **2015**, 7, 2055.
[115] M. Choi, C. Kim, S. Ok Jeon, K. Soo Yook, J. Yeob Lee, J. Jang, Chem. Commun., **2011**, 47, 7092.
[116] S.H. Hwang, J. Yun, J. Jang, Adv. Funct. Mater., **2014**, 24, 7619.
[117] D. Bi, S.J. Moon, L. Häggman, G. Boschloo, L. Yang, E.M.J. Johansson, M.K. Nazeeruddin, M. Grätzel, A. Hagfeldt, RSC Advances, **2013**, 3, 18762.
[118] S.H. Hwang, J. Roh, J. Lee, J. Ryu, J. Yun, J. Jang, J. Mater. Chem. A, **2014**, 2, 16429.
[119] J.M. Ball, M.M. Lee, A. Hey, H.J. Snaith, Energy and Environmental Science, **2013**, 6, 1739.
[120] P. Schulz, E. Edri, S. Kirmayer, G. Hodes, D. Cahen, A. Kahn, Energy & Environmental Science, **2014**, 7, 1377.
[121] Y. Gao, Y. Masuda, Z. Peng, T. Yonezawa, K. Koumoto, J. Mater. Chem., **2003**, 13, 608.
[122] F. Gracia, F. Yubero, J.P. Holgado, J.P. Espinos, A.R. Gonzalez-Elipe, T. Girardeau, Thin Solid Films, **2006**, 500, 19.
[123] U. Bach, D. Lupo, P. Comte, J.E. Moser, F. Weissortel, J.

Salbeck, H. Spreitzer, M. Gratzel, Nature, **1998**, 395, 583.
[124] Y.B. Zheng, S.J. Wang, A.C.H. Huan, C.Y. Tan, L. Yan, C.K. Ong, Appl. Phys. Lett., **2005**, 86, 112910.
[125] S. Liu, G. Liu, Q. Feng, J Porous Mater, **2010**, 17, 197.
[126] W. Li, H. Dong, X. Guo, N. Li, J. Li, G. Niu, L. Wang, J. Mater. Chem. A, **2014**, 2, 20105.
[127] J. Li, W. Li, H. Dong, N. Li, X. Guo, L. Wang, J. Mater. Chem. A, **2015**, 3, 8882.
[128] H.-S. Kim, I. Mora-Sero, V. Gonzalez-Pedro, F. Fabregat-Santiago, E.J. Juarez-Perez, N.-G. Park, J. Bisquert, Nat Commun, **2013**, 4.
[129] S.K. Pathak, A. Abate, P. Ruckdeschel, B. Roose, K.C. Gödel, Y. Vaynzof, A. Santhala, S.-I. Watanabe, D.J. Hollman, N. Noel, A. Sepe, U. Wiesner, R. Friend, H.J. Snaith, U. Steiner, Adv. Funct. Mater., **2014**, 24, 6046.
[130] H.-H. Wang, Q. Chen, H. Zhou, L. Song, Z.S. Louis, N.D. Marco, Y. Fang, P. Sun, T.-B. Song, H. Chen, Y. Yang, J. Mater. Chem. A, **2015**, 3, 9108.
[131] D. Zhao, C. Chen, Y. Wang, W. Ma, J. Zhao, T. Rajh, L. Zang, Environmental Science & Technology, **2008**, 42, 308.
[132] J.H. Kim, J.S. Kim, H. Choi, S.M. Lee, B.H. Jun, K.N. Yu, E. Kuk, Y.K. Kim, D.H. Jeong, M.H. Cho, Y.S. Lee, Anal. Chem., **2006**, 78, 6967.
[133] Y. Ma, W. Li, E.C. Cho, Z. Li, T. Yu, J. Zeng, Z. Xie, Y. Xia, ACS Nano, **2010**, 4, 6725.
[134] N.G. Park, J. Van De Lagemaat, A.J. Frank, J. Phys. Chem. B, **2000**, 104, 8989.
[135] J.B. Joo, I. Lee, M. Dahl, G.D. Moon, F. Zaera, Y. Yin, Adv. Funct. Mater., **2013**, 23, 4246.
[136] X. Zhang, H. Wang, Z. Su, Langmuir, **2012**, 28, 15705.

[137] E. Prodan, C. Radloff, N.J. Halas, P. Nordlander, Science, **2003**, 302, 419.
[138] D.D. Evanoff Jr, G. Chumanov, ChemPhysChem, **2005**, 6, 1221.
[139] H. Baida, P. Billaud, S. Marhaba, D. Christofilos, E. Cottancin, A. Crut, J. Lermé, P. Maioli, M. Pellarin, M. Broyer, N. Del Fatti, F. Vallée, A. Sánchez-Iglesias, I. Pastoriza-Santos, L.M. Liz-Marzán, Nano Lett., **2009**, 9, 3463.
[140] J. Qi, X. Dang, P.T. Hammond, A.M. Belcher, ACS Nano, **2011**, 5, 7108.
[141] H.J. Son, X. Wang, C. Prasittichai, N.C. Jeong, T. Aaltonen, R.G. Gordon, J.T. Hupp, J. Am. Chem. Soc., **2012**, 134, 9537.
[142] J. Yun, S.H. Hwang, J. Jang, ACS Applied Materials & Interfaces, **2015**, 7, 2055.
[143] D. Hulicova-Jurcakova, M. Seredych, G.Q. Lu, T.J. Bandosz, Adv. Funct. Mater., **2009**, 19, 438.
[144] Z.-H. Sheng, L. Shao, J.-J. Chen, W.-J. Bao, F.-B. Wang, X.-H. Xia, ACS Nano, **2011**, 5, 4350.
[145] D. Zhou, L. Yang, L. Yu, J. Kong, X. Yao, W. Liu, Z. Xu, X. Lu, Nanoscale, **2015**, 7, 1501.
[146] S. Chen, J. Bi, Y. Zhao, L. Yang, C. Zhang, Y. Ma, Q. Wu, X. Wang, Z. Hu, Adv. Mater., **2012**, 24, 5593.
[147] T. Sharifi, G. Hu, X. Jia, T. Wågberg, ACS Nano, **2012**, 6, 8904.
[148] T. Xing, Y. Zheng, L.H. Li, B.C.C. Cowie, D. Gunzelmann, S.Z. Qiao, S. Huang, Y. Chen, ACS Nano, **2014**, 8, 6856.
[149] P. Simon, Y. Gogotsi, B. Dunn, Science, **2014**, 343, 1210.
[150] D.S. Su , R. Schlögl, ChemSusChem, **2010**, 3, 136.
[151] F. Su, C.K. Poh, J.S. Chen, G. Xu, D. Wang, Q. Li, J. Lin, X.W. Lou, Energy & Environmental Science, **2011**, 4, 717.
[152] J. Han, G. Xu, B. Ding, J. Pan, H. Dou, D.R. MacFarlane, J. Mater. Chem. A, **2014**, 2, 5352.

[153] G.A. Ferrero, M. Sevilla, A.B. Fuertes, Carbon, **2015**, 88, 239.
[154] B. Qiu, C. Pan, W. Qian, Y. Peng, L. Qiu, F. Yan, J. Mater. Chem. A, **2013**, 1, 6373.
[155] L. Zhao, L.-Z. Fan, M.-Q. Zhou, H. Guan, S. Qiao, M. Antonietti, M.-M. Titirici, Adv. Mater., **2010**, 22, 5202.
[156] A. Chen, Y. Li, Y. Yu, S. Ren, Y. Wang, K. Xia, S. Li, J. Alloys Compd., **2016**, 688, Part A, 878.

국문초록

재료 공학 분야에서 나노물질은 우수한 물성과 성능을 통해 기존의 분야를 개발하거나 새로운 분야를 개척하는 소재로 사용되고 있다. 특히, 중공 나노구조체는 높은 표면적, 낮은 밀도, 담지능력, 광산란 능력을 가지고 있어서 나노 과학 및 기술분야에 많은 관심을 끌고 있다. 이러한 중공구조 나노구조체를 제조하는 방법에는 편리한 템플레잇 방법을 많이 사용하고 있으며 그 외에도 다양한 접근법으로 제조하고 있다. 하지만, 사이즈와 형태를 조절하거나 균일하게 제조 해야하는 문제가 존재한다. 또한, 응용분야의 필요성에 맞춰 복합물질을 제조하거나 기능을 추가하는 연구가 필요한 실정이다.

본 학위 논문에서는 무기 중공구조 나노구조체를 제조와 이의 에너지 변환·저장 소재로의 응용에 대해 서술하고 있다. 실리카와 이산화티타늄 기반의 중공구조 나노입자는 졸-겔 방법으로 제조하였다. 또한, 질소가 도핑된 이중 셸 중공구조 나노입자의 경우 졸-겔방법으로 실리카/이산화티타늄 이중 셸 중공구조 나노입자를 제조한 뒤, 템플레잇 방법으로

제조하였다. 이렇게 제조된 실리카/이산화티타늄 기반의 중공구조 나노입자는 염료감응형 태양전지와 페로브스카이트 태양전지의 소재로써 응용하였다. 중공구조 나노입자가 가지는 넓은 표면적과 광산란 효과 및 로딩의 원활함을 사용하였고 중공구조의 조성에 따른 전자 이동 효과를 이용하였다. 질소가 도핑된 이중 구조의 탄소 나노입자는 슈퍼캐패시터의 소재재로 응용하였다. 이중 구조의 넓은 표면적과 질소 도핑으로 인한 산화 환원 반응으로 인해 성능향상을 도모하였다. 결과적으로 본 논문에서 제시된 방법을 통해 제조된 무기 중공 나노구조체는 에너지 변환·저장 응용 분야의 이해를 높이고 성능을 향상 시켰다.

주요어: 나노입자, 무기 나노구조체, 중공구조체, 태양전지, 슈퍼캐패시터,